NATIONAL ENERGY TECHNOLOGY LABORATORY

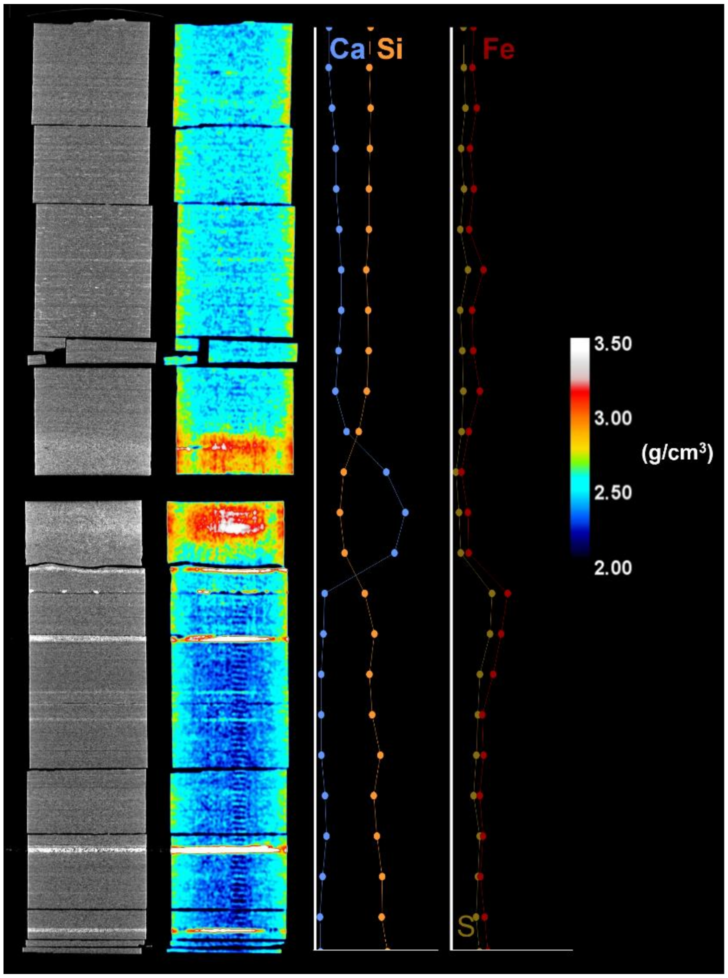

Computed Tomography Scanning and Geophysical Measurements of Core from the Boggess 17H Well

12 January 2022

U.S. DEPARTMENT OF ENERGY

NATIONAL ENERGY TECHNOLOGY LABORATORY

Office of Fossil Energy

DOE/NETL-2022/3723

Disclaimer

Cover Illustration: Data from the Boggess 17H at depths of 7,950 to 7,953 ft. Image of medical computed tomography (CT) scan (left), dual energy density image with scale bar in g/cm on the far right (middle), and select X-ray fluorescence (XRF) data (right).

Suggested Citation: Paronish, T.; Schmitt, R.; Crandall, D.; Moore, J.; Brown, S.; Carr, T., Panetta, B.; *Computed Tomography Scanning and Geophysical Measurements of Core from the Boggess 17H Well*; DOE.NETL-2022.3723; NETL Technical Report Series; U.S. Department of Energy, National Energy Technology Laboratory: Morgantown, WV, 2022; p 44. DOI: 10.2172/1839669

An electronic version of this report can be found at: https://netl.doe.gov/energy-analysis/search

The data in this report can be accessed from NETL's Energy Data eXchange (EDX) online system (https://edx.netl.doe.gov) using the following link: https://edx.netl.doe.gov/dataset/boggess-17h-well

Computed Tomography Scanning and Geophysical Measurements of Core from the Boggess 17H Well

Thomas Paronish[1,2], Rhiannon Schmitt[1,3], Paige Mackey[1,3], Dustin Crandall[1], Johnathan Moore[1,2], Sarah Brown[1,2], Tim Carr[4], Brian Panetta[4]

[1]U.S. Department of Energy, National Energy Technology Laboratory,
3610 Collins Ferry Road, Morgantown, WV 26507

[2]NETL Support Contractor, 3610 Collins Ferry Road, Morgantown, WV 26507

[3]U.S. Department of Energy, Oak Ridge Institute for Science and Education (ORISE), 3610 Collins Ferry Road, Morgantown, WV 26507

[4]West Virginia University, Department of Geology and Geography, 98 Beechurst Avenue, Morgantown, WV 26506

DOE/NETL-2022/3723

12 January 2022

NETL Contacts:

Dustin Crandall, Principal Investigator

Christina Lopano and Eilis Rosenbaum, Technical Portfolio Lead

Bryan Morreale, Executive Director, Research & Innovation Center

Table of Contents

ABSTRACT......1

1. INTRODUCTION......2

1.1 SITE OVERVIEW......2

1.2 SEDIMENTATION AND STRATIGRAPHY......3

2. CORE DESCRIPTION......5

2.1 CORE PHOTOGRAPHS......9

3. DATA ACQUISITION AND METHODOLOGY......13

3.1 MEDICAL CT SCANNING......13

3.2 MULTI-SENSOR CORE LOGGING......14

4. RESULTS......18

4.1 MEDICAL CT SCANS......18

4.2 BOGGESS 17H CORE SAMPLES......19

4.3 ADDITIONAL CT DATA......27

4.4 DUAL ENERGY CT SCANNING......28

4.5 COMPILED CORE LOG......30

5. DISCUSSION......33

6. REFERENCES......35

This page intentionally left blank.

List of Figures

Figure 1: Map showing MSEEL wells drilled to the Marcellus Shale. Purple star indicates pad locations and black dots indicate lateral terminations. At the MIP pad, there were 4 horizontal wells and a vertical monitoring well drilled just outside Morgantown, WV. Boggess 17H well is located on the Boggess pad northwest of the MIP pad consists of 6 horizontal wells and a vertical pilot well. 2

Figure 2: (A) Structure map for the top of the Marcellus Shale, the black dot denotes the study area and sits 6,000 ft below mean sea level; (B) Marcellus isopach map, the black dot denotes the study area. Generally, the Marcellus Shale decreases in thickness from approximately 300 ft in the east to about 25 ft in the west. 4

Figure 3: Generalized core description for Boggess 17H. 8

Figure 4: Photographs of core from the Boggess 17H well, (left) 7,873 to 7,883 ft and (right) 7,883 to 7,893 ft. 9

Figure 5: Photographs of core from the Boggess 17H well, (left) 7,893 to 7,900.35 ft and (right) 7,905 to 7,915 ft. 9

Figure 6: Photographs of core from the Boggess 17H well, (left) 7,915 to 7,925 ft and (right) 7,925 to 7,935 ft. 10

Figure 7: Photographs of core from the Boggess 17H well, (left) 7,935 to 7,945 ft and (right) 7,945 to 7,955 ft. 10

Figure 8: Photographs of core from the Boggess 17H well, (left) 7,955 to 7,956.7 ft and (right) 7,957 to 7,967 ft. 11

Figure 9: Photographs of core from the Boggess 17H well, (left) 7,967 to 7,977 ft and (right) 7,977 to 7,987 ft. 11

Figure 10: Photographs of core from the Boggess 17H well, (left) 7,987 to 7,997 ft and (right) 7,997 to 8,007 ft. 12

Figure 11: Photographs of core from the Boggess 17H well, 8,007 to 8,017 ft. 12

Figure 12: Toshiba® Aquilion™ Multislice Helical CT scanner at NETL used for core analysis. 13

Figure 13: MSCL allows researchers to continuously run petrophysical measurements on whole core: (A) natural gamma detector; (B) XRF spectrometry sensor; (C) magnetic susceptibility loop sensor; (D) magnetic susceptibility point sensor; (E) P-wave velocity transducers; (F) gamma density source, and non-contacting electrical resistivity sensor (not shown). 14

Figure 14: Periodic table showing elements measurable for each suite (Mining-Plus, Mining, and Soil) by the Innov-X® XRF spectrometer. 17

Figure 15: Schematic of the XZ isolated plane through the vertical center of the medical CT scans of the Boggess 17H core. 18

Figure 16: 2D isolated planes through the vertical center of the medical CT scans of the Boggess 17H core from 7,873 to 7,891 ft. 19

Figure 17: 2D isolated planes through the vertical center of the medical CT scans of the Boggess 17H core from 7,891 to 7,911 ft. 20

Figure 18: 2D isolated planes through the vertical center of the medical CT scans of the Boggess 17H core from 7,911 to 7,925.7 ft. 21

Figure 19: 2D isolated planes through the vertical center of the medical CT scans of the Boggess 17H core from 7,925.7 to 7,947ft. 22

List of Figures (cont.)

Figure 20: 2D isolated planes through the vertical center of the medical CT scans of the Boggess 17H core from 7,947 to 7,963 ft. 23
Figure 21: 2D isolated planes through the vertical center of the medical CT scans of the Boggess 17H core from 7,963 to 7,981 ft. 24
Figure 22: 2D isolated planes through the vertical center of the medical CT scans of the Boggess 17H core from 7,981 to 7,999 ft. 25
Figure 23: 2D isolated planes through the vertical center of the medical CT scans of the Boggess 17H core from 7,999 to 8,017 ft. 26
Figure 24: 2D isolated planes through the vertical center of the medical CT scans of the Boggess 17H core from 8,017 to 8,017.5 ft. 27
Figure 25: Single image from a video file available on EDX showing variation in the Boggess 17H core from 7,876 to 7,879 ft. This shows the variation in composition within the matrix perpendicular to the core length in this case highlighting burrows in a carbonate interval. Note the bright (high density) concretions in the matrix. 27
Figure 26: Photon interactions at varying energies: A) Photoelectric absorption, B) Compton scattering. 28
Figure 27: Compiled core log detailing the elemental results; Marcellus Shale (blue), Onondaga Limestone (purple), and Huntersville Chert (orange).. 31
Figure 28: Compiled core log of elemental ratios; Marcellus Shale (blue), Onondaga Limestone (purple), and Huntersville Chert (orange).. 32

List of Tables

Table 1: SESAR IGSN Sample Names 5
Table 2: Magnetic Susceptibility Values for Common Minerals 15
Table 3: List of Sidewall Plug CT Images.. 28
Table 4: Dual Energy Calibration Standards, Bulk Density (gm/cm^3).. 29
Table 5: Dual Energy Calibration Standards, HU, and CTN for “Low” and “High” Energies.... 29

Acronyms, Abbreviations, and Symbols

Term	Description
2D	Two-dimensional
3D	Three-dimensional
API	American Petroleum Institute
BBL	Billion barrels
CT	Computed tomography
CTN	CT numbers
DOE	U.S. Department of Energy
EDX	NETL's Energy Data eXchange
HU	Hounsfield Units
IGSN	International Geo Sample Number
MSCL	Multi-Sensor Core Logger
MSEEL	Marcellus Shale Energy and Environment Laboratory
NETL	National Energy Technology Laboratory
ORISE	Oak Ridge Institute for Science and Education
SESAR	System for Earth Science Sample Registration
Tcf	Trillion cubic feet
TOC	Total organic carbon
XRF	X-ray fluorescence

Acknowledgments

This work was completed at the National Energy Technology Laboratory (NETL) with support from U.S. Department of Energy's (DOE) Office of Fossil Energy Oil & Gas Program. The authors wish to acknowledge Bryan Morreale (NETL Research & Innovation Center), Jared Ciferno (NETL Technology Development and Integration Center), and Olayinka Ogunsola (DOE Office of Fossil Energy) for programmatic guidance, direction, and support.

The authors would like to thank Scott Workman for data collection and technical support. This research was supported in part by appointments from the NETL Research Participation Program, sponsored by the U.S. DOE and administered by the Oak Ridge Institute for Science and Education (ORISE).

ABSTRACT

The computed tomography (CT) facilities and the Multi-Sensor Core Logger (MSCL) at the National Energy Technology Laboratory (NETL) in Morgantown, West Virginia were used to characterize the Marcellus Shale and underlying formations. The core is from a vertical pilot well (Boggess 17H) drilled in western Monongalia County near Core, West Virginia by Northeast Natural Energy for the second Marcellus Shale Energy and Environmental Laboratory (MSEEL). MSEEL is a joint venture between NETL, Northeast Natural Energy, and West Virginia University. The primary impetus for this report is to characterize the core to better understand the structure and variation of the Marcellus Shale and surrounding formations. This report, and the associated scans, provide detailed datasets not typically available from unconventional shales for analysis. The resultant datasets are presented as part of this report and can be accessed from NETL's Energy Data eXchange (EDX) online system (https://edx.netl.doe.gov) using the following link: https://edx.netl.doe.gov/dataset/boggess-17h-well.

All equipment and techniques used were non-destructive, enabling future examinations to be performed on these cores. None of the equipment used was suitable for direct visualization of the shale pore space, although fractures and discontinuities were detectable with the methods tested. CT imagery with the NETL medical CT scanner was performed on the entire core. Qualitative analysis of the medical CT images, coupled with X-ray fluorescence (XRF), P-wave, and magnetic susceptibility measurements from the MSCL were useful in identifying zones of interest for more detailed analysis and locating fractured zones. The ability to quickly identify key areas for more detailed study with higher resolution will save time and resources in future studies. The combination of all methods used provides a multi-scale analysis of the core; the resulting macro and micro descriptions of the core are relevant for many subsurface energy related examinations of core that have traditionally been performed at NETL.

1. INTRODUCTION

The Middle Devonian Marcellus Shale has become one of the most prolific shale plays in the world with the development of hydraulic fracturing and horizontal drilling. The Marcellus play has a lateral extent of 21,266 mi^2 (55,078.7 km^2) in the Appalachian basin and has an estimated technically recoverable resource of 309.0 trillion cubic feet (Tcf) of natural gas with an additional 14.0 billion barrels (BBL) of natural gas liquids (EIA, 2018). Given the potential of the Marcellus Shale as a long-term major producer of gas and gas liquids, it is important to better understand and utilize best practices to identify and produce the resource economically and to do so in an environmentally responsible manner. Under these principles, the Marcellus Shale Energy and Environmental Laboratory (MSEEL) project was founded to pursue a better understanding of the Marcellus Shale by utilizing new technologies to optimize production and reduce the environmental impact. The MSEEL project is a joint venture between the U.S. Department of Energy's (DOE) National Energy Technology Laboratory (NETL), West Virginia University, and Northeast Natural Energy.

1.1 SITE OVERVIEW

The project site is located on the Boggess Pad outside Core, West Virginia approximately 7 mi. (11 km) northwest of the MIP-3H Pad (Figure 1). The Boggess pad consists of 6 lateral wells and a vertical pilot well. The Boggess 17H pilot and lateral (API 47-061-01812) is the focus for this report. Similar analyses found in this report were conducted on the MIP-3H well (Paronish et al., 2018) and the associated data can be found on EDX (Crandall, 2018) and MSEEL.org.

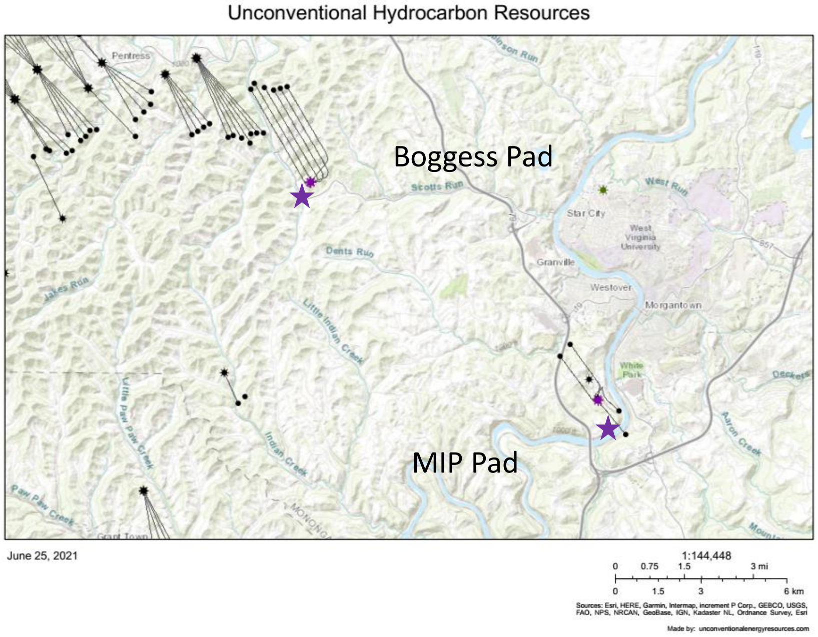

Figure 1: Map showing MSEEL wells drilled to the Marcellus Shale. Purple star indicates pad locations and black dots indicate lateral terminations. At the MIP pad, there were 4 horizontal wells and a vertical monitoring well drilled just outside Morgantown, WV. Boggess 17H well is located on the Boggess pad northwest of the MIP pad consists of 6 horizontal wells and a vertical pilot well (http://www.mseel.org/viewer/).

The Boggess 17H well (API 47-061-01812) geographic coordinates are: latitude 39.66645° N, longitude -80.09689° W. The Marcellus Shale is approximately 100 ft (30.5 m) thick and occurs at a measured depth of approximately 7,873 ft (2,399.69 m). Approximately 139 ft of core was recovered from the Boggess 17H well at a depth from 7,873 ft to 8,016 ft (2,399.7 to 2,443.3 m); this encompasses strata from the Huntersville to the lower portion of the Mahantango.

1.2 SEDIMENTATION AND STRATIGRAPHY

The Boggess 17H project's primary focus is on the Marcellus Shale. The Marcellus Shale is a Middle Devonian (Eifelian to Givetian) mudstone at the base of the Hamilton Group. The Marcellus Shale is underlain by the crystalline Onondaga Limestone and Huntersville Chert and overlain by the clay-rich dark grey shale of the Mahantango Formation, also included in this report.

The Marcellus Shale in the study area is expected to be found at a depth of approximately 6,200 ft (1889.76 m) from mean sea level and to be approximately 100 ft (30.5 m) thick (Figure 2).

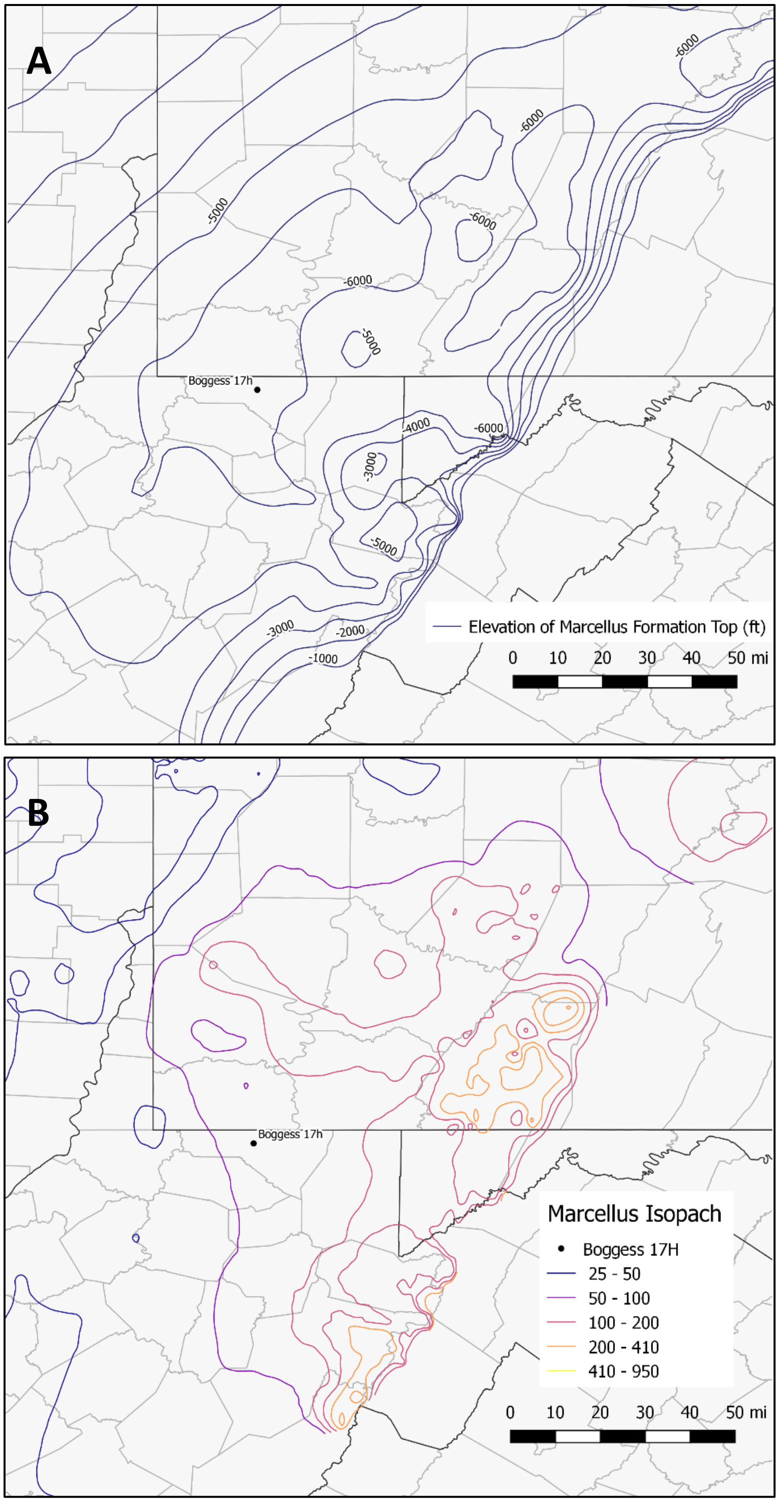

Figure 2: (A) Structure map for the top of the Marcellus Shale, the black dot denotes the study area and sits 6,000 ft below mean sea level; (B) Marcellus isopach map, the black dot denotes the study area. Generally, the Marcellus Shale decreases in thickness from approximately 300 ft in the east to about 25 ft in the west.

2. CORE DESCRIPTION

The methods established for fine-grained sedimentary rocks by Lazar et al. (2015) were used to describe the Boggess 17H core. The core was described in two passes, the first focused on determining “texture” and “composition”. Texture refers to the amount of silt-sized quartz grains present and is defined as coarse, medium, or fine silt-sized grains. Composition of the mudstone is defined by the amount of quartz, carbonate, and clay present and is categorized as siliceous, calcareous, and argillaceous, respectively. The second description focused on sedimentary and structural features present in the core. These features include the identification of fracture type and intensity, nodules, concretions, bedding, other fabric, fossils, and bioturbation (Lazar et al., 2015). The second pass was aided by the medical computed tomography (CT) scans to identify fracture structures and morphology in a three-dimensional (3D) prospective.

The Boggess 17H core was described from 7,908 to 8,012 ft (Figure 3). The Onondaga Limestone is described from 7,972 to 8,012 ft, and is primarily made up of medium to light gray crystalline limestone with zones of dark gray shale and dark gray chert. The Marcellus Shale overlies this interval. This interval is defined by medium dark gray to dark gray, clay-rich shale, transitioning into dark gray to black, siliceous, organic-rich shale, becoming calcareous and fossil-rich at the base of the Marcellus Shale. Fine to medium silt-sized quartz is present with minor calcite cement with some pyrite replacement.

These cores were entered in the System for Earth Science Sample Registration (SESAR), a registry that catalogs and preserves sample data and allows access for industry, academic institutes, researchers, and the public to view this data online (IEDA, 2018). Each core box is assigned an International Geo Sample Number (IGSN) which allows unique identification and referencing. These listings for the Boggess 17H well are shown in Table 1 and via the parent link (https://app.geosamples.org/sample/igsn/IENTLBOGG).

Table 1: SESAR IGSN Sample Names

Field Name	IGSN	Link
MSEEL2 Bog 1/3rd C1 B1	IENTL01BK	https://app.geosamples.org/sample/igsn/IENTL01BK
MSEEL2 Bog 1/3rd C1 B2	IENTL01BL	https://app.geosamples.org/sample/igsn/IENTL01BKL
MSEEL2 Bog 1/3rd C1 B3	IENTL01BM	https://app.geosamples.org/sample/igsn/IENTL01BM
MSEEL2 Bog 1/3rd C2 B1	IENTL01BN	https://app.geosamples.org/sample/igsn/IENTL01BN
MSEEL2 Bog 1/3rd C2 B2	IENTL01BO	https://app.geosamples.org/sample/igsn/IENTL01BO
MSEEL2 Bog 1/3rd C2 B3	IENTL01BP	https://app.geosamples.org/sample/igsn/IENTL01BP
MSEEL2 Bog 1/3rd C2 B4	IENTL01BQ	https://app.geosamples.org/sample/igsn/IENTL01BQ
MSEEL2 Bog 1/3rd C2 B5	IENTL01BR	https://app.geosamples.org/sample/igsn/IENTL01BR
MSEEL2 Bog 1/3rd C2 B6	IENTL01BS	https://app.geosamples.org/sample/igsn/IENTL01BS
MSEEL2 Bog 1/3rd C3 B1	IENTL01BT	https://app.geosamples.org/sample/igsn/IENTL01BT
MSEEL2 Bog 1/3rd C3 B2	IENTL01BU	https://app.geosamples.org/sample/igsn/IENTL01BU
MSEEL2 Bog 1/3rd C3 B3	IENTL01BV	https://app.geosamples.org/sample/igsn/IENTL01BV

Table 1: SESAR IGSN Sample Names (cont.)

Field Name	IGSN	Link
MSEEL2 Bog 1/3rd C3 B4	IENTL01BW	https://app.geosamples.org/sample/igsn/IENTL01BW
MSEEL2 Bog 1/3rd C3 B5	IENTL01BX	https://app.geosamples.org/sample/igsn/IENTL01BX
MSEEL2 Bog 1/3rd C3 B6	IENTL01BY	https://app.geosamples.org/sample/igsn/IENTL01BY
MSEEL2 Bog C1 B1	IENTL01BZ	https://app.geosamples.org/sample/igsn/IENTL01BZ
MSEEL2 Bog C1 B2	IENTL01C0	https://app.geosamples.org/sample/igsn/IENTL01C0
MSEEL2 Bog C1 B3	IENTL01C1	https://app.geosamples.org/sample/igsn/IENTL01C1
MSEEL2 Bog C1 B4	IENTL01C2	https://app.geosamples.org/sample/igsn/IENTL01C2
MSEEL2 Bog C1 B5	IENTL01C3	https://app.geosamples.org/sample/igsn/IENTL01C3
MSEEL2 Bog C1 B6	IENTL01C4	https://app.geosamples.org/sample/igsn/IENTL01C4
MSEEL2 Bog C1 B7	IENTL01C5	https://app.geosamples.org/sample/igsn/IENTL01C5
MSEEL2 Bog C1 B8	IENTL01C6	https://app.geosamples.org/sample/igsn/IENTL01C6
MSEEL2 Bog C1 B9	IENTL01C7	https://app.geosamples.org/sample/igsn/IENTL01C7
MSEEL2 Bog C1 B10	IENTL01C8	https://app.geosamples.org/sample/igsn/IENTL01C8
MSEEL2 Bog C2 B1	IENTL01C9	https://app.geosamples.org/sample/igsn/IENTL01C9
MSEEL2 Bog C2 B2	IENTL01CA	https://app.geosamples.org/sample/igsn/IENTL01CA
MSEEL2 Bog C2 B3	IENTL01CB	https://app.geosamples.org/sample/igsn/IENTL01CB
MSEEL2 Bog C2 B4	IENTL01CC	https://app.geosamples.org/sample/igsn/IENTL01CC
MSEEL2 Bog C2 B5	IENTL01CD	https://app.geosamples.org/sample/igsn/IENTL01CD
MSEEL2 Bog C2 B6	IENTL01CE	https://app.geosamples.org/sample/igsn/IENTL01CE
MSEEL2 Bog C2 B7	IENTL01CF	https://app.geosamples.org/sample/igsn/IENTL01CF
MSEEL2 Bog C2 B8	IENTL01CG	https://app.geosamples.org/sample/igsn/IENTL01CG
MSEEL2 Bog C2 B9	IENTL01CH	https://app.geosamples.org/sample/igsn/IENTL01CH
MSEEL2 Bog C2 B10	IENTL01CI	https://app.geosamples.org/sample/igsn/IENTL01CI
MSEEL2 Bog C2 B11	IENTL01CJ	https://app.geosamples.org/sample/igsn/IENTL01CJ
MSEEL2 Bog C2 B12	IENTL01CK	https://app.geosamples.org/sample/igsn/IENTL01CK
MSEEL2 Bog C2 B13	IENTL01CL	https://app.geosamples.org/sample/igsn/IENTL01CL
MSEEL2 Bog C2 B14	IENTL01CM	https://app.geosamples.org/sample/igsn/IENTL01CM
MSEEL2 Bog C2 B15	IENTL01CN	https://app.geosamples.org/sample/igsn/IENTL01CN
MSEEL2 Bog C2 B16	IENTL01CO	https://app.geosamples.org/sample/igsn/IENTL01CO
MSEEL2 Bog C2 B17	IENTL01CP	https://app.geosamples.org/sample/igsn/IENTL01CP
MSEEL2 Bog C2 B18	IENTL01CQ	https://app.geosamples.org/sample/igsn/IENTL01CQ
MSEEL2 Bog C3 B1	IENTL01CR	https://app.geosamples.org/sample/igsn/IENTL01CR

Table 1: SESAR IGSN Sample Names (cont.)

Field Name	IGSN	Link
MSEEL2 Bog C3 B2	IENTL01CS	https://app.geosamples.org/sample/igsn/IENTL01CS
MSEEL2 Bog C3 B3	IENTL01CT	https://app.geosamples.org/sample/igsn/IENTL01CT
MSEEL2 Bog C3 B4	IENTL01CU	https://app.geosamples.org/sample/igsn/IENTL01CU
MSEEL2 Bog C3 B5	IENTL01CV	https://app.geosamples.org/sample/igsn/IENTL01CV
MSEEL2 Bog C3 B6	IENTL01CW	https://app.geosamples.org/sample/igsn/IENTL01CW
MSEEL2 Bog C3 B7	IENTL01CX	https://app.geosamples.org/sample/igsn/IENTL01CX
MSEEL2 Bog C3 B8	IENTL01CY	https://app.geosamples.org/sample/igsn/IENTL01CY
MSEEL2 Bog C3 B9	IENTL01CZ	https://app.geosamples.org/sample/igsn/IENTL01CZ
MSEEL2 Bog C3 B10	IENTL01D0	https://app.geosamples.org/sample/igsn/IENTL01D0
MSEEL2 Bog C3 B11	IENTL01D1	https://app.geosamples.org/sample/igsn/IENTL01D1
MSEEL2 Bog C3 B12	IENTL01D2	https://app.geosamples.org/sample/igsn/IENTL01D2
MSEEL2 Bog C3 B13	IENTL01D3	https://app.geosamples.org/sample/igsn/IENTL01D3
MSEEL2 Bog C3 B14	IENTL01D4	https://app.geosamples.org/sample/igsn/IENTL01D4
MSEEL2 Bog C3 B15	IENTL01D5	https://app.geosamples.org/sample/igsn/IENTL01D5
MSEEL2 Bog C3 B16	IENTL01D6	https://app.geosamples.org/sample/igsn/IENTL01D6
MSEEL2 Bog C3 B17	IENTL01D7	https://app.geosamples.org/sample/igsn/IENTL01D7
MSEEL2 Bog C3 B18	IENTL01D8	https://app.geosamples.org/sample/igsn/IENTL01D8
MSEEL2 Bog C3 B19	IENTL01D9	https://app.geosamples.org/sample/igsn/IENTL01D9
MSEEL2 Bog C3 B20	IENTL01DA	https://app.geosamples.org/sample/igsn/IENTL01DA
MSEEL2 Bog C3 B21	IENTL01DB	https://app.geosamples.org/sample/igsn/IENTL01DB

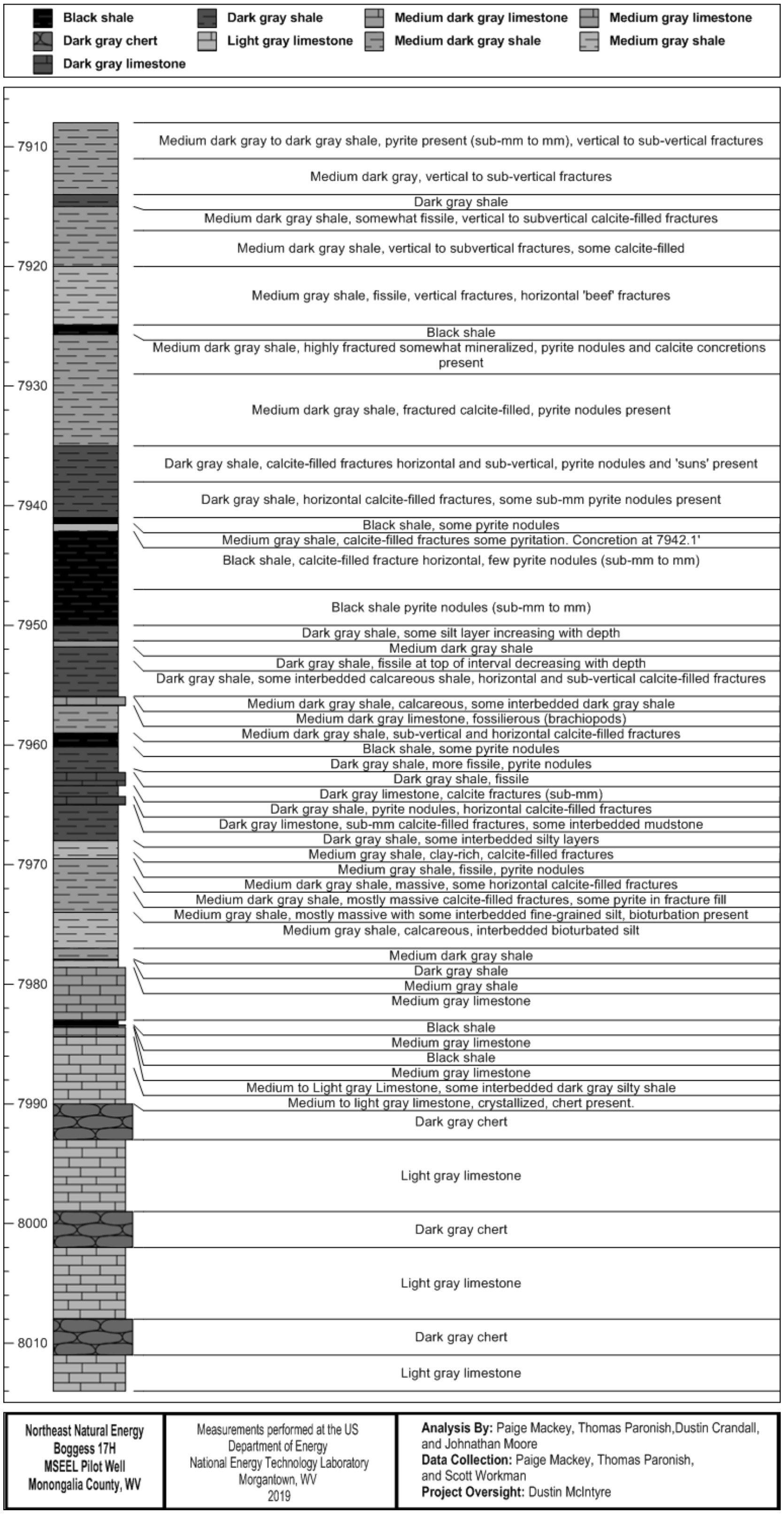

Figure 3: Generalized core description for Boggess 17H.

2.1 CORE PHOTOGRAPHS

Core photographs for Boggess 17H from 7,873 to 8,017 ft (Figure 4 to Figure 11).

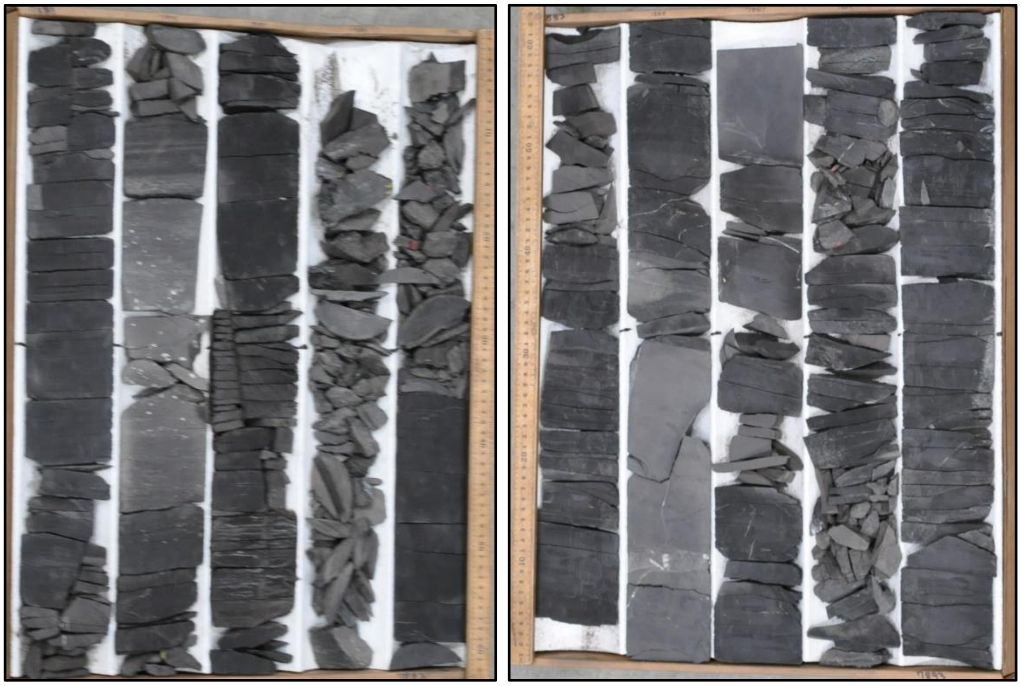

Figure 4: Photographs of core from the Boggess 17H well, (left) 7,873 to 7,883 ft and (right) 7,883 to 7,893 ft.

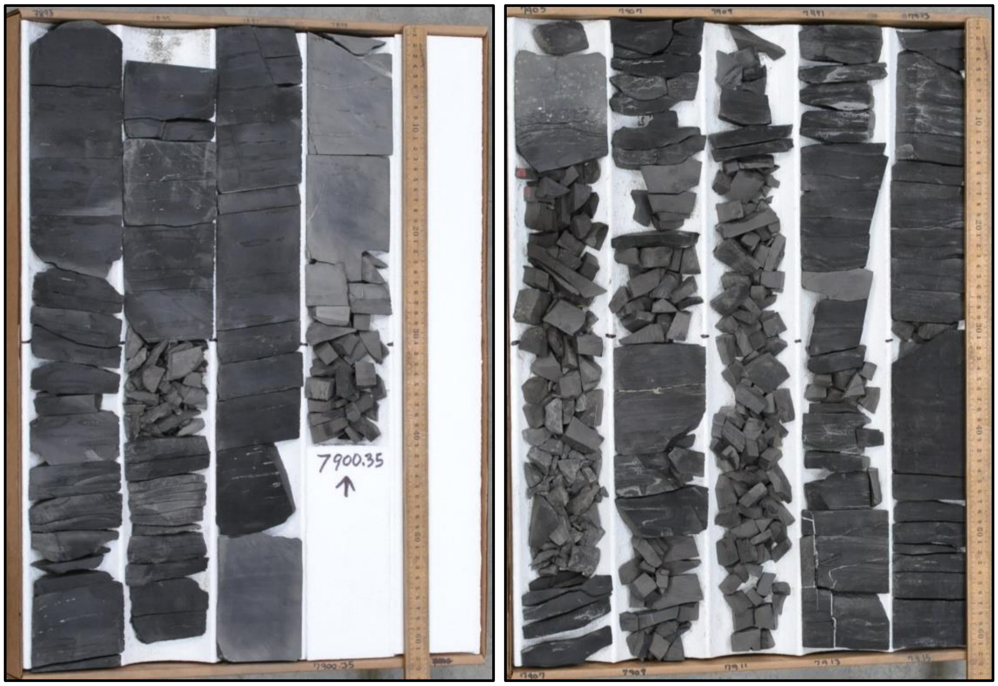

Figure 5: Photographs of core from the Boggess 17H well, (left) 7,893 to 7,900.35 ft and (right) 7,905 to 7,915 ft.

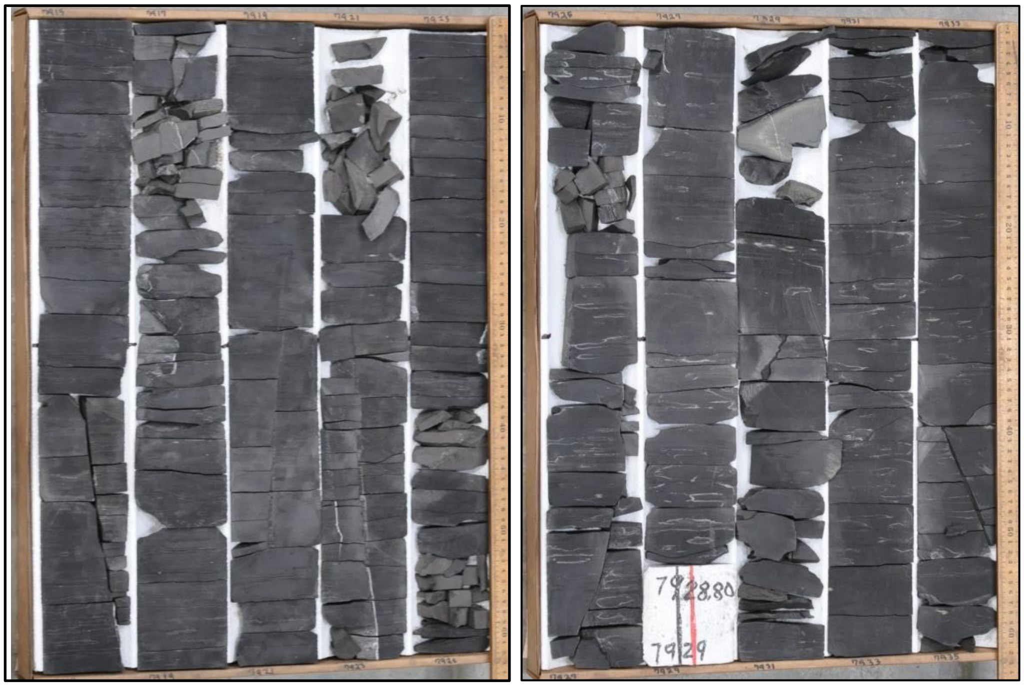

Figure 6: Photographs of core from the Boggess 17H well, (left) 7,915 to 7,925 ft and (right) 7,925 to 7,935 ft.

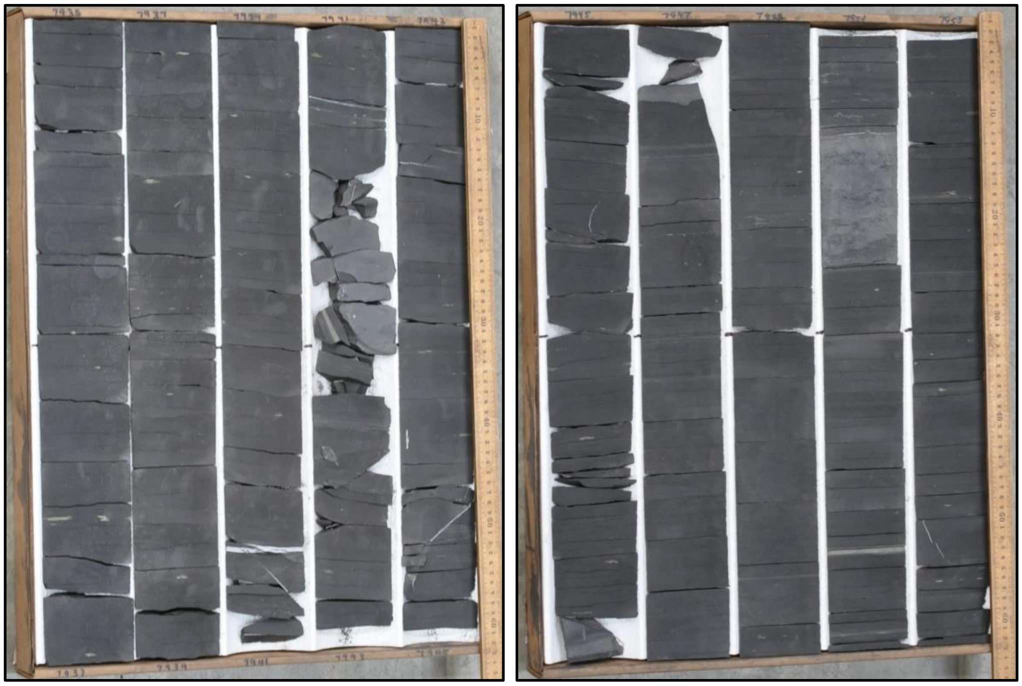

Figure 7: Photographs of core from the Boggess 17H well, (left) 7,935 to 7,945 ft and (right) 7,945 to 7,955 ft.

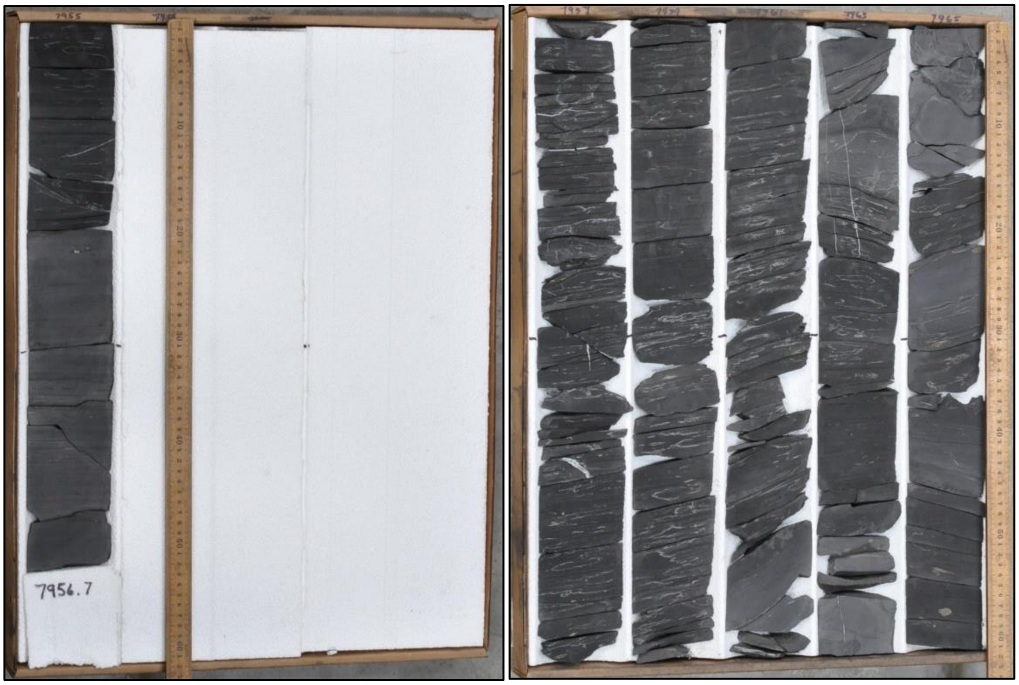

Figure 8: Photographs of core from the Boggess 17H well, (left) 7,955 to 7,956.7 ft and (right) 7,957 to 7,967 ft.

Figure 9: Photographs of core from the Boggess 17H well, (left) 7,967 to 7,977 ft and (right) 7,977 to 7,987 ft.

Figure 10: Photographs of core from the Boggess 17H well, (left) 7,987 to 7,997 ft and (right) 7,997 to 8,007 ft.

Figure 11: Photographs of core from the Boggess 17H well, 8,007 to 8,017 ft.

3. DATA ACQUISITION AND METHODOLOGY

The samples were evaluated using medical CT scanning and geophysical and geochemical core logging. Medical CT scanning and core logging were performed over the entire length of the core.

3.1 MEDICAL CT SCANNING

The entire Boggess 17H core was scanned with a Toshiba® Aquilion TSX-101A/R medical scanner shown in Figure 12. The medical CT scanner generates images with a resolution in the millimeter range, with scans having voxel resolutions of 0.43 x 0.43 mm in the XY plane and 0.50 mm along the core axis. All scans were performed through the core barrels obtained in ~3 ft or smaller sections. The scans were conducted at a voltage of 135 kV and at 200 mA with a data collection diameter of 220 mm and using the helical detector rotation/acquisition. Subsequent processing and combining of stacks were performed to create 3D volumetric representations of the cores and a two-dimensional (2D) cross-section through the middle of the core samples. The CT scans were exported as DICOM images by the proprietary Toshiba® software and combined into 16-bit tif stacks using ImageJ (Rasband, 2019). The variation in greyscale values observed in these CT images indicates changes in the CT number obtained from the CT scans, which is directly proportional to changes in the attenuation and density of the scanned rock. Lower density regions are represented as darker greyscale values, and higher density regions are represented with brighter greyscale images.

Figure 12: Toshiba® Aquilion™ Multislice Helical CT scanner at NETL used for core analysis.

3.2 MULTI-SENSOR CORE LOGGING

Geophysical measurements of core thickness deviation, P-wave travel time, P-wave signal amplitude, magnetic susceptibility, and attenuated gamma counts were obtained with a Geotek® Multi-Sensor Core Logging (MSCL) system. Geotek® MSCL software was used to process the raw data into core thickness, P-wave velocity, gamma density, and fractional porosity values. Additionally, the system was used to measure bulk elemental chemistry with a built-in, portable X-ray fluorescence (XRF) spectrometer. The Geotek® MSCL system at the NETL has many additional capabilities, however only those that were significant to this characterization are described in the following sections (Figure 13).

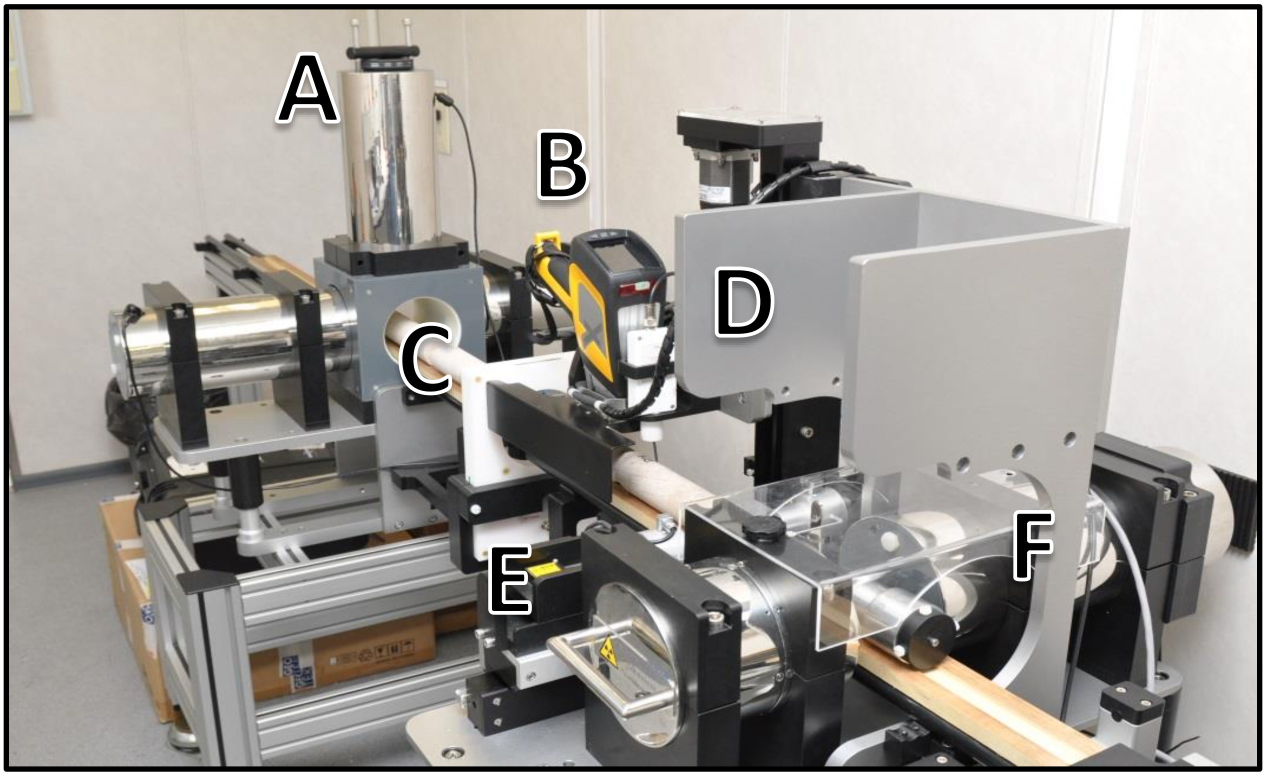

Figure 13: MSCL allows researchers to continuously run petrophysical measurements on whole core: (A) natural gamma detector; (B) XRF spectrometry sensor; (C) magnetic susceptibility loop sensor; (D) magnetic susceptibility point sensor; (E) P-wave velocity transducers; (F) gamma density source, and non-contacting electrical resistivity sensor (not shown).

3.2.1 P-wave Velocity

P-wave velocity measurements were performed to measure the acoustic impedance of a geologic sample with compressional waves. Acoustic impedance is a measure of how well a material transmits vibrations, which is directly proportional to density and/or material consolidation. An example of a material that has a high acoustic impedance is air, with a wave speed of 330 m/s, whereas granite has low acoustic impedance, with a wave speed of > 5,000 m/s. These measurements can be proxies for seismic reflection coefficients and can be translated to field use when doing seismic surveys.

The software associated with the MSCL measures the travel time of the pulse with a resolution of 50 ns. The absolute accuracy of the instrument measurements is ± 3 m/s with a resolution of 1.5 m/s (Geotek Ltd. Multi-Sensor Core Logger Manual, Version 05-10; Geotek Ltd., 2010).

3.2.2 Magnetic Susceptibility

Magnetic susceptibility is a measure of the degree of magnetization in a sample. The sample is exposed to an external magnetic field and magnetic susceptibility is the measured magnetic response to that field:

$$J = kH$$

Where, J is the magnetic response (per unit volume), k is volume susceptibility, and H is an external magnetic field. The measurement unit is dimensionless (abbreviated simply as SI).

All materials have magnetic susceptibility. Positive values of magnetic susceptibility indicate that materials are paramagnetic and occur in rocks that consist of the majority ferromagnetic, ferrimagnetic, or antimagnetic (iron bearing) materials. Negative values of magnetic susceptibility indicate that materials are diamagnetic and occur in rocks dominated by non-iron material (i.e., calcite or quartz). Table 1 lists examples of common magnetic susceptibility ranges (Hunts et al., 1995).

Magnetic susceptibility was measured using a Bartington point sensor, where a 1-cm diameter, low intensity (8.0 A/m RMS), non-sensitive, alternating magnetic field (2 kHz) was generated for 10 s. To minimize any potential drift in the oscillating field the point sensor was zeroed at the beginning and end of the sample, as well as, after every 5th measurement. The point sensor, due to the small field, was limited in whole core measurements, and additionally was temperature dependent (Geotek Ltd. Multi-Sensor Core Logger Manual, Version 05-10; Geotek Ltd., 2010).

Table 2: Magnetic Susceptibility Values for Common Minerals (Hunts et al., 1995)

Mineral	X ($*10^{-6}$) SI
Water	9
Calcite	-7.5 to -39
Halite, Gypsum	-10 to -60
Illite, Montmorillonite	330 to 410
Pyrite	5 to 3,500
Hematite	500 to 40,000
Magnetite	1,000,000 to 5,700,000

3.2.3 Gamma Density

Gamma density was acquired by subjecting the sample to gamma radiation and then measuring the attenuation of that radiation. The attenuation is directly proportional to the density of the sample and is acquired by measuring the difference between radiation energy at the emission source and after it passes through the sample. Specifically, the MSCL software calculates the bulk density, ρ, by using the following equation:

$$\rho = \left(\frac{1}{\mu d}\right) \ln\left(\frac{I_o}{I}\right)$$

Where μ = Compton attenuation coefficient, d = thickness, I_o = source intensity, and I = measured intensity.

3.2.4 X-ray Fluorescence Spectrometry

In addition to the geophysical measurements, a portable handheld Innov-X® XRF was used to measure relative elemental abundances. The Mining-plus suite was run at 6 cm resolution at an exposure time of 60 s per beam.

The Mining-Plus suite utilizes a 2-beam analysis that resolves primarily major elements (Mg, Al, Si, P, S, Cl, Fe, K, Ca, and Ti), minor elements (V, Cu, Ni, Cr, Mn, and Pb), trace elements (Co, Zn, As, Zr, Mo, Ag, Cd, Sn, Sb, Hf, W, and Bi), and an aggregated “light element” (H to Na) (Figure 14). The mining-plus suite resolve elemental abundances that are reported relative to the total elemental composition, i.e., out of 100% weight.

The XRF spectrometer measures elemental abundances by subjecting the sample to X-ray photons. The high energy of the photons displaces inner orbital electrons in the respective elements. The vacancies in the lower orbitals cause outer orbital electrons to “fall” into lower orbits to satisfy the disturbed electron configuration. The substitution into lower orbitals causes a release of a secondary X-ray photon, which has an energy associated with a specific element. These relative and element specific energy emissions can then be used to determine bulk elemental composition.

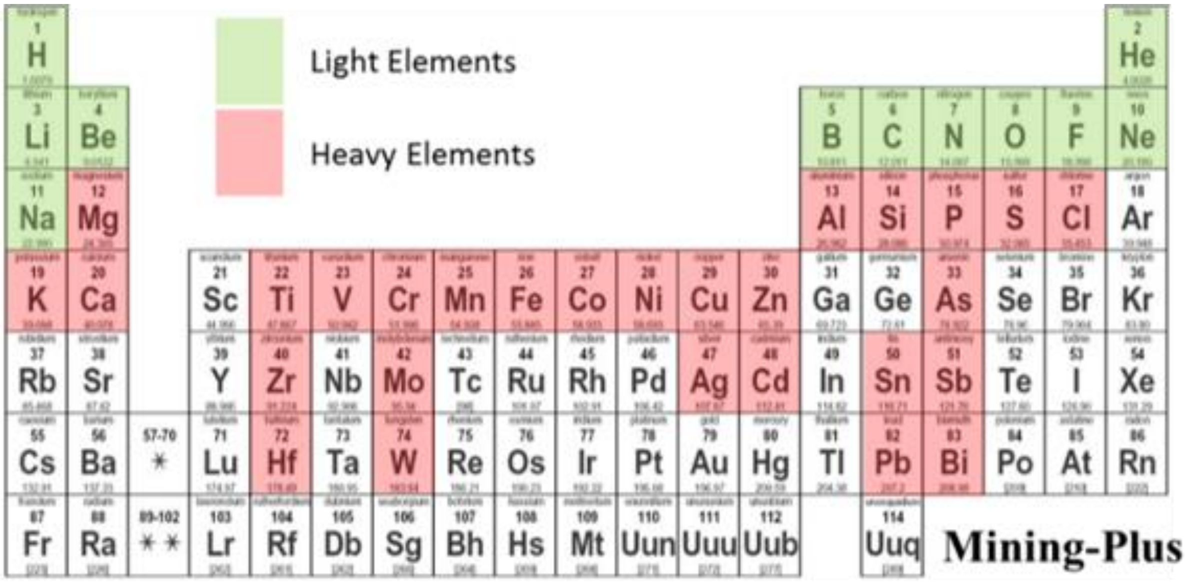

Figure 14: Periodic table showing elements measurable for each suite (Mining-Plus, Mining, and Soil) by the Innov-X® XRF spectrometer.

4. RESULTS

The following section contains the data obtained from the medical CT and the MSCL scans of the core obtained from Boggess 17H well.

4.1 MEDICAL CT SCANS

Processed 2D slices of the medical CT scans through the cores are shown first, followed by various analyses of fractures and variations in the shale structure observed from the medical CT scans. As previously discussed, the variation in greyscale observed in the medical CT images indicate changes in the CT number obtained, which is directly proportional to changes in the attenuation and density of the scanned rock. Darker regions are less dense zones with lower X-ray attenuation (e.g., gas filled fractures) and lighter regions are more dense zones with higher X-ray attenuation. Very highly attenuating materials within the core (e.g., pyrite nodules) resulted in streaking CT artifacts (Cnudde and Boone, 2013) which are visible in the following images as white/bright rays emanating from the rock.

4.1.1 XZ Planes

A 2D image through the center of each retrieved core barrel can be found in Figure 16 through Figure 24. These are referred to as “XZ” planes with the coordinates that are shown in Figure 15. There is no scale bar shown in these images; the retrieved core has a diameter of 4 in. (10.16 cm) for reference. The labels below each 2D XZ plane in Figure 16 through Figure 24 are the depth at the bottom of each core; the full range of core lengths shown in each figure is listed in the figure captions. The greyscale values were shifted in these images to best represent the structure of the core in each image.

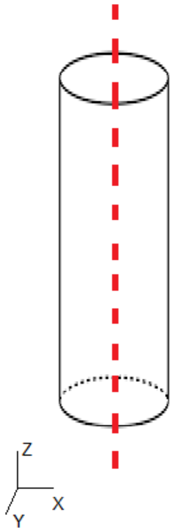

Figure 15: Schematic of the XZ isolated plane through the vertical center of the medical CT scans of the Boggess 17H core.

4.2 BOGGESS 17H CORE SAMPLES

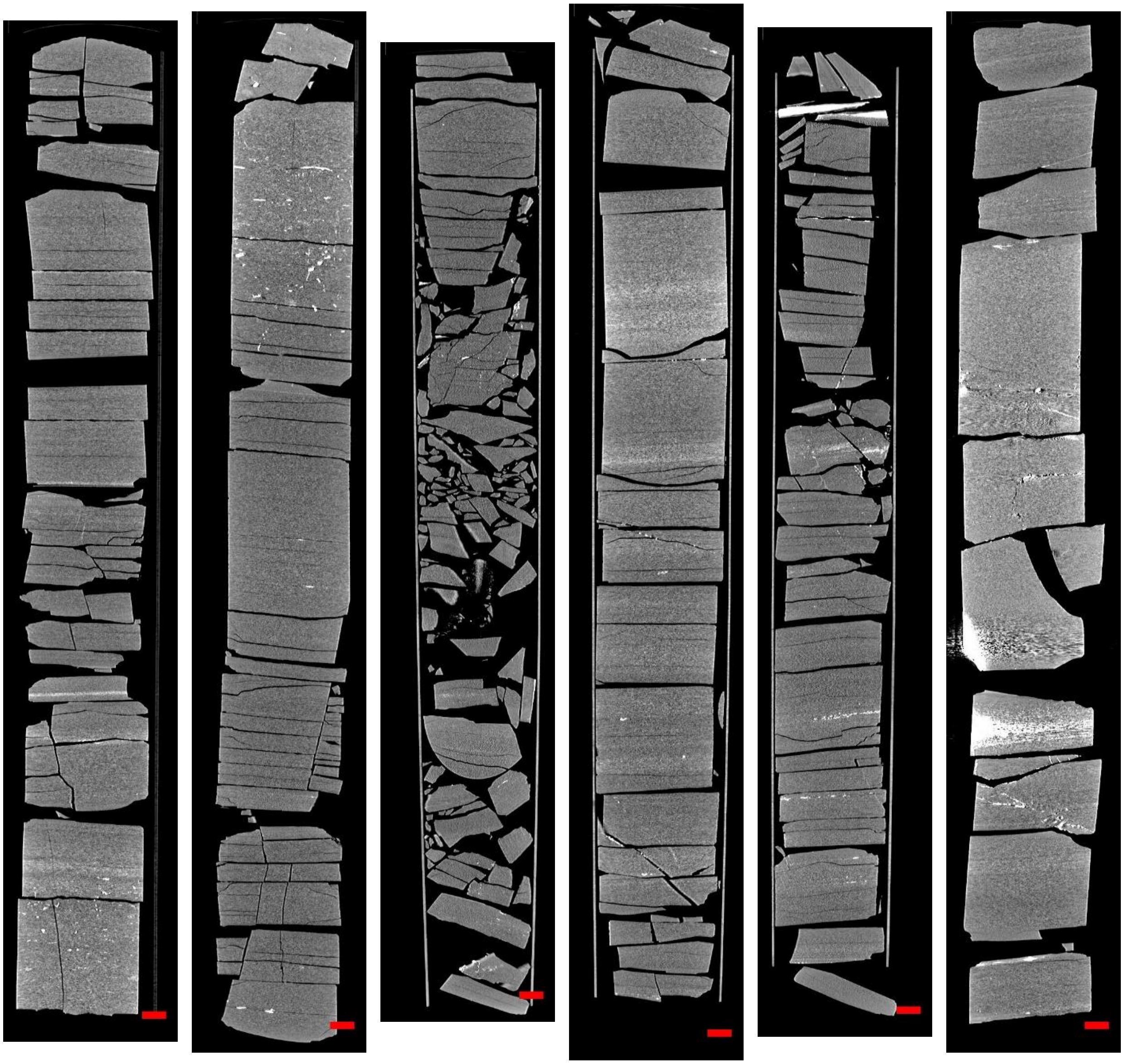

7,873–7,876 ft **7,876–7,879 ft** **7,879–7,882 ft** **7,882–7,885 ft** **7,885–7,888 ft** **7,888–7,891 ft**

Figure 16: 2D isolated planes through the vertical center of the medical CT scans of the Boggess 17H core from 7,873 to 7,891 ft.

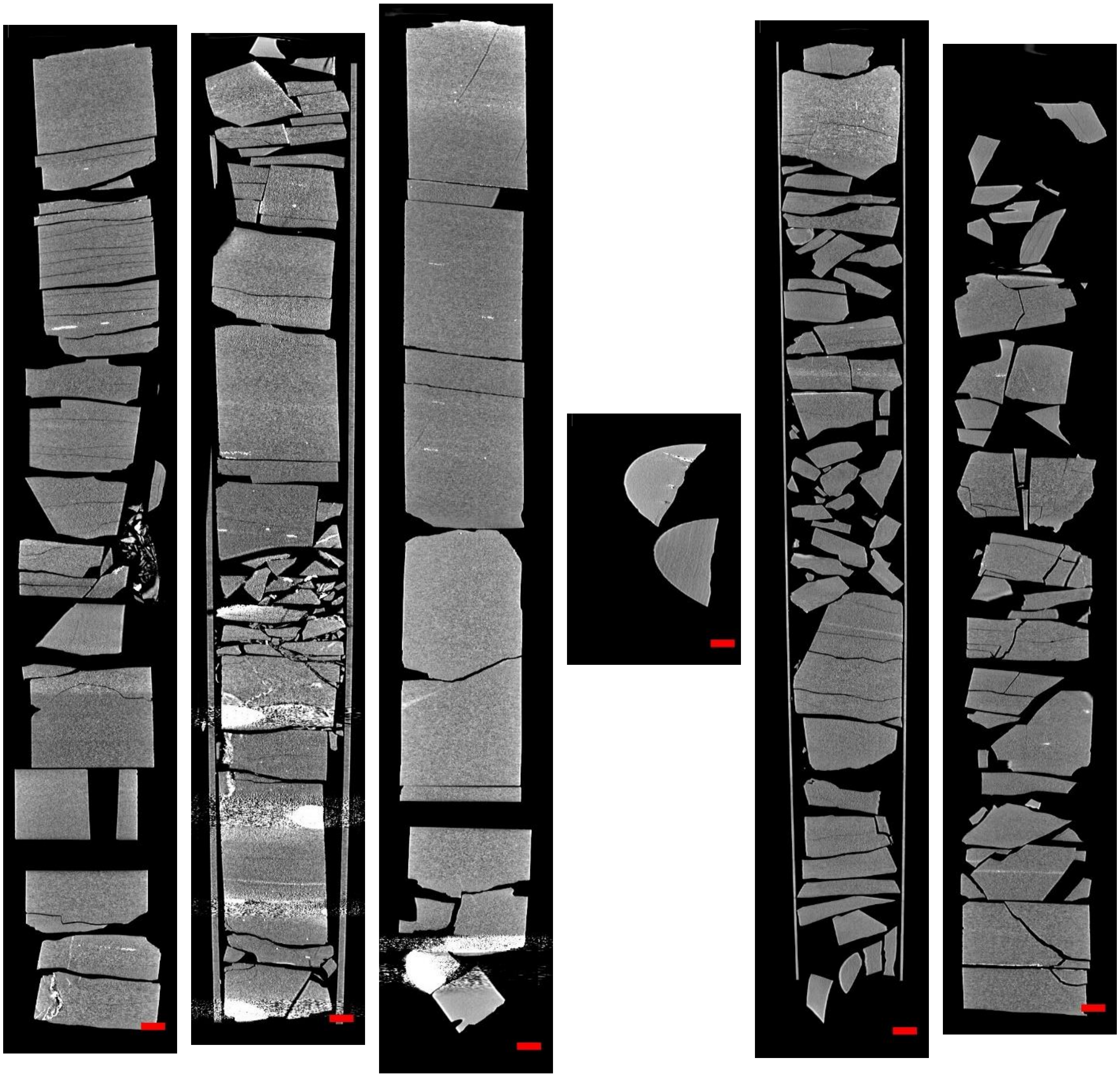

7,891–7,894 ft **7,894–7,897 ft** **7,897–7,900 ft** **7,900–7,901 ft** **7,905–7,908 ft** **7,908–7,911 ft**

Figure 17: 2D isolated planes through the vertical center of the medical CT scans of the Boggess 17H core from 7,891 to 7,911 ft.

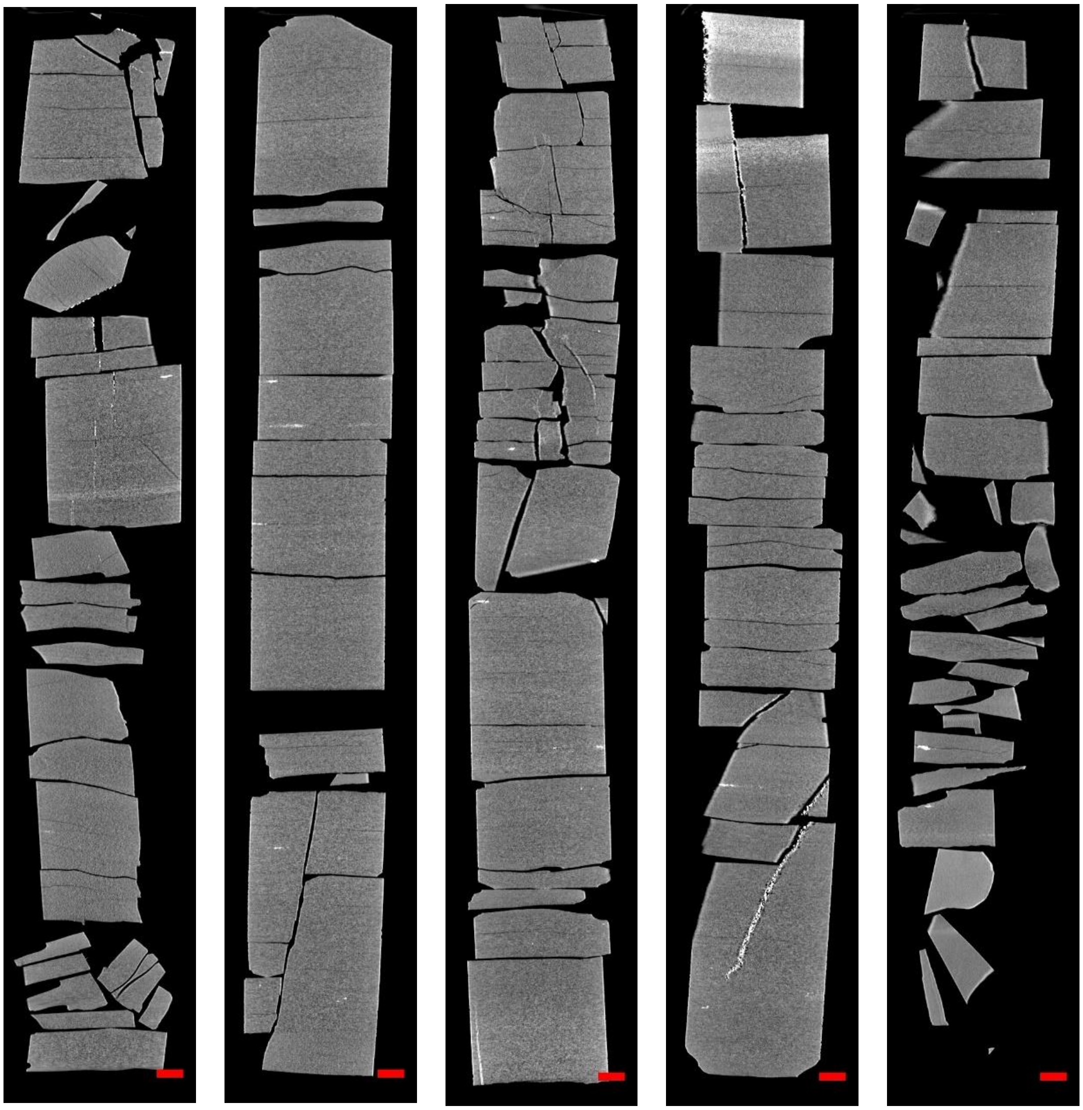

7,911–7,914 ft **7,914–7,917 ft** **7, 917–7,920 ft** **7,920–7,923 ft** **7,923–7,926 ft**

Figure 18: 2D isolated planes through the vertical center of the medical CT scans of the Boggess 17H core from 7,911 to 7,925.7 ft.

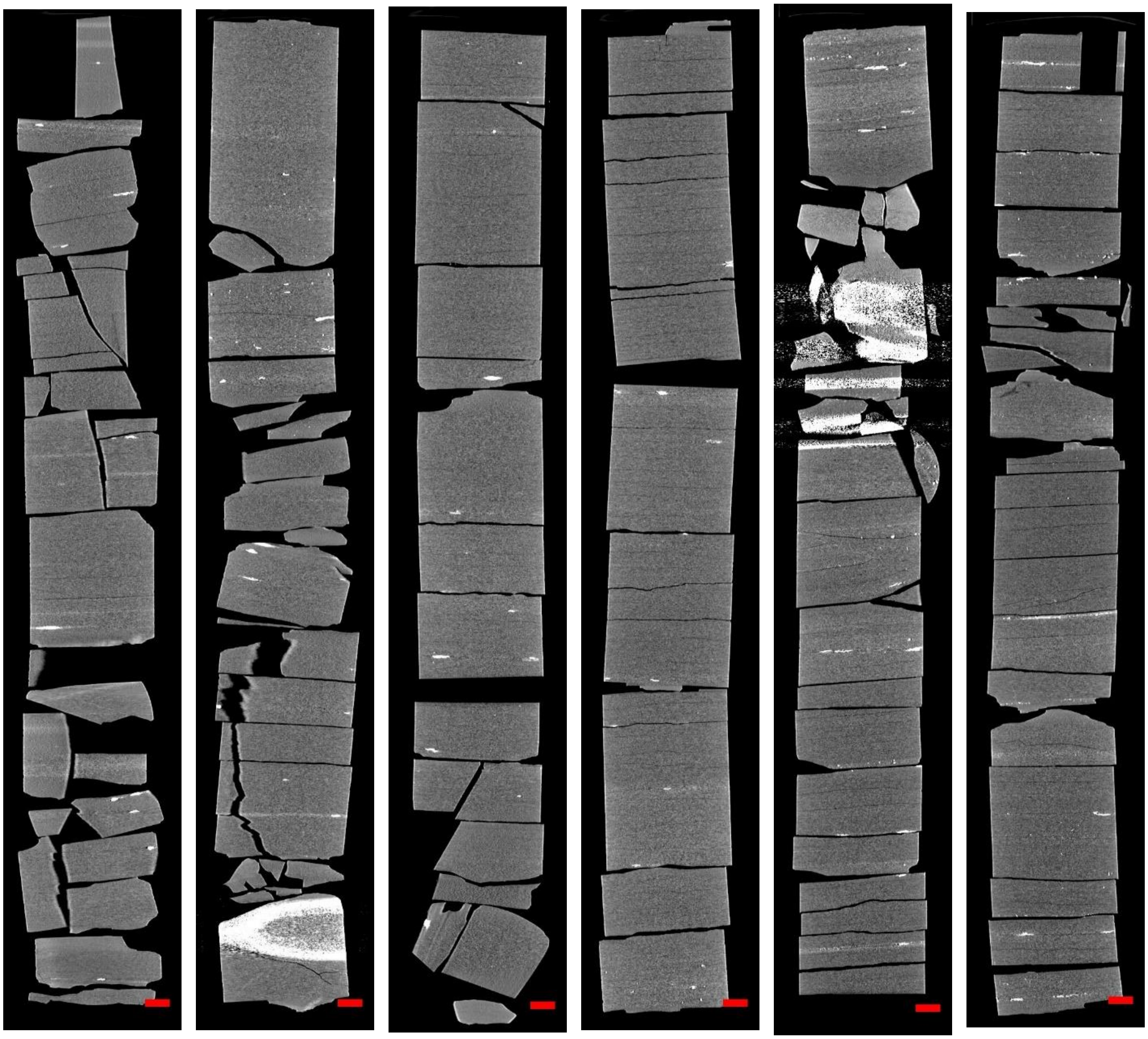

7,926–7,929 **7,929–7,932 ft** **7,932–7,935 ft** **7,935–7,938 ft** **7,941–7,944 ft** **7,944–7,947 ft**

Figure 19: 2D isolated planes through the vertical center of the medical CT scans of the Boggess 17H core from 7,925.7 to 7,947ft.

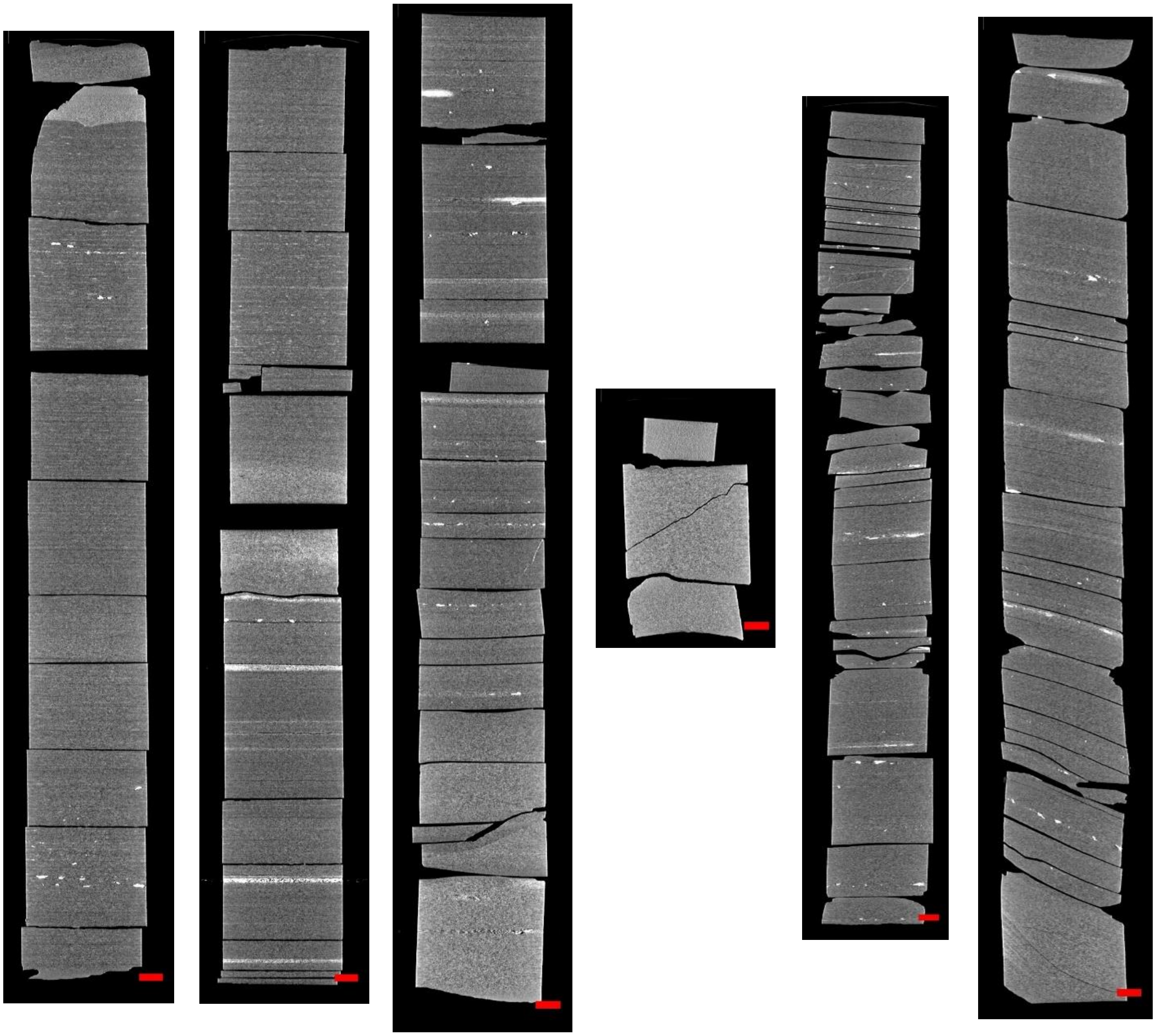

7,947–7,950 ft **7,950–7,953 ft** **7,953–7,956 ft** **7,956–7,956.7 ft** **7,957–7,960 ft** **7,960–7,963 ft**

Figure 20: 2D isolated planes through the vertical center of the medical CT scans of the Boggess 17H core from 7,947 to 7,963 ft.

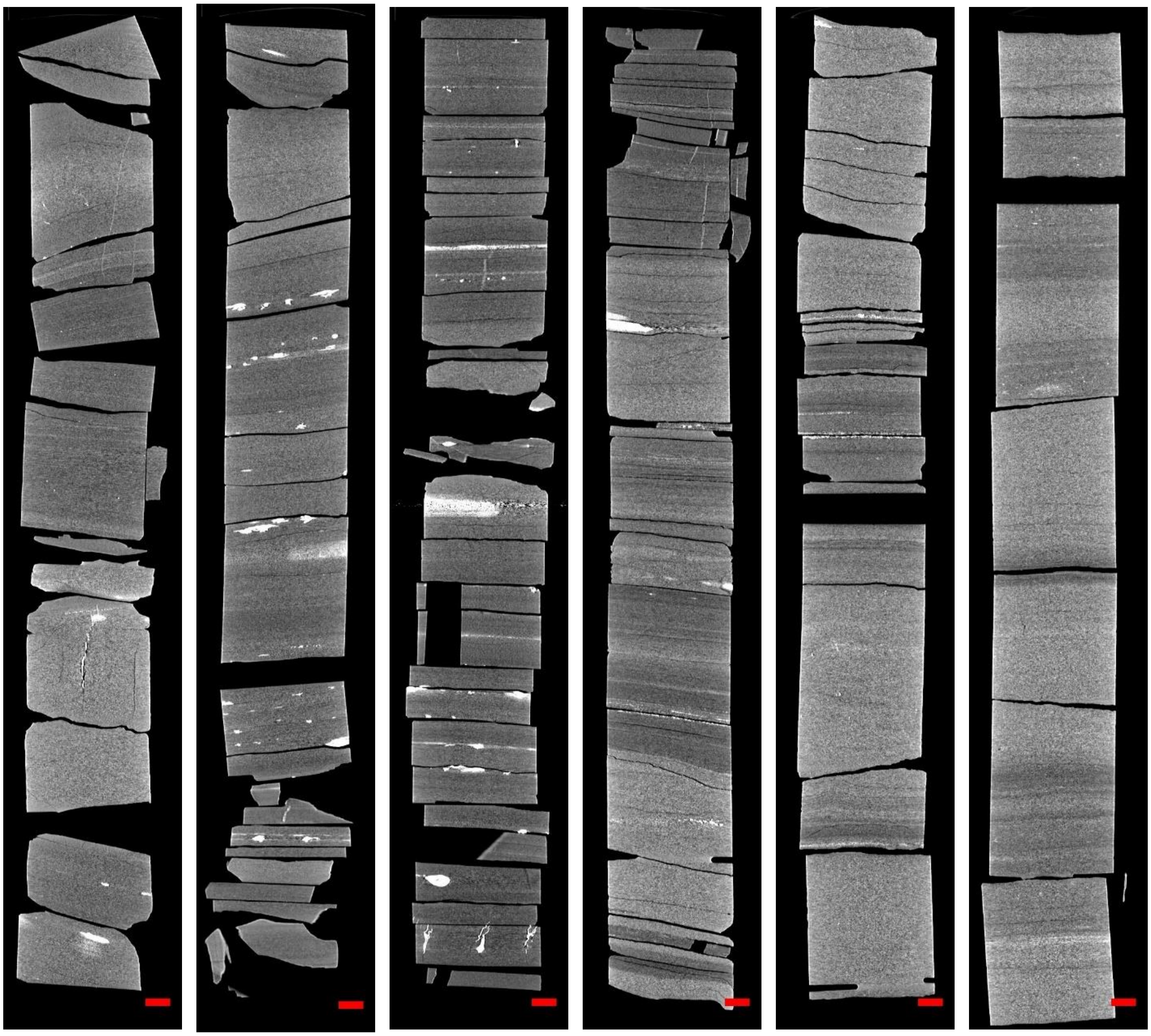

7,963–7,966 ft **7,966–7,969 ft** **7,969–7,972 ft** **7,972–7,975 ft** **7,975–7,978 ft** **7,978–7,981 ft**

Figure 21: 2D isolated planes through the vertical center of the medical CT scans of the Boggess 17H core from 7,963 to 7,981 ft.

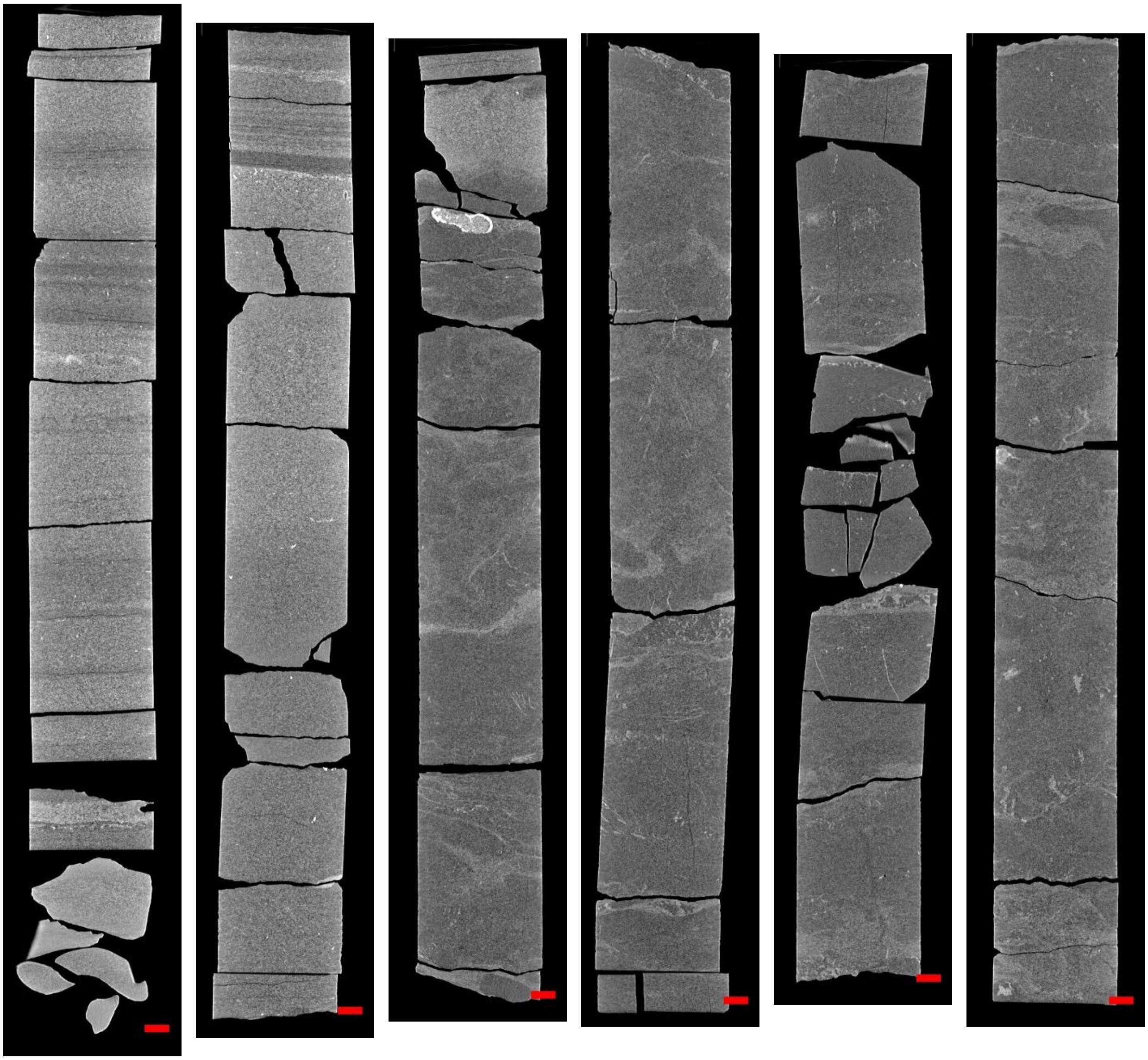

7,981–7,984 ft **7,984.4–7,987 ft** **7,987–7,990 ft** **7,990–7,993 ft** **7,993–7,996 ft** **7,996–7,999 ft**

Figure 22: 2D isolated planes through the vertical center of the medical CT scans of the Boggess 17H core from 7,981 to 7,999 ft.

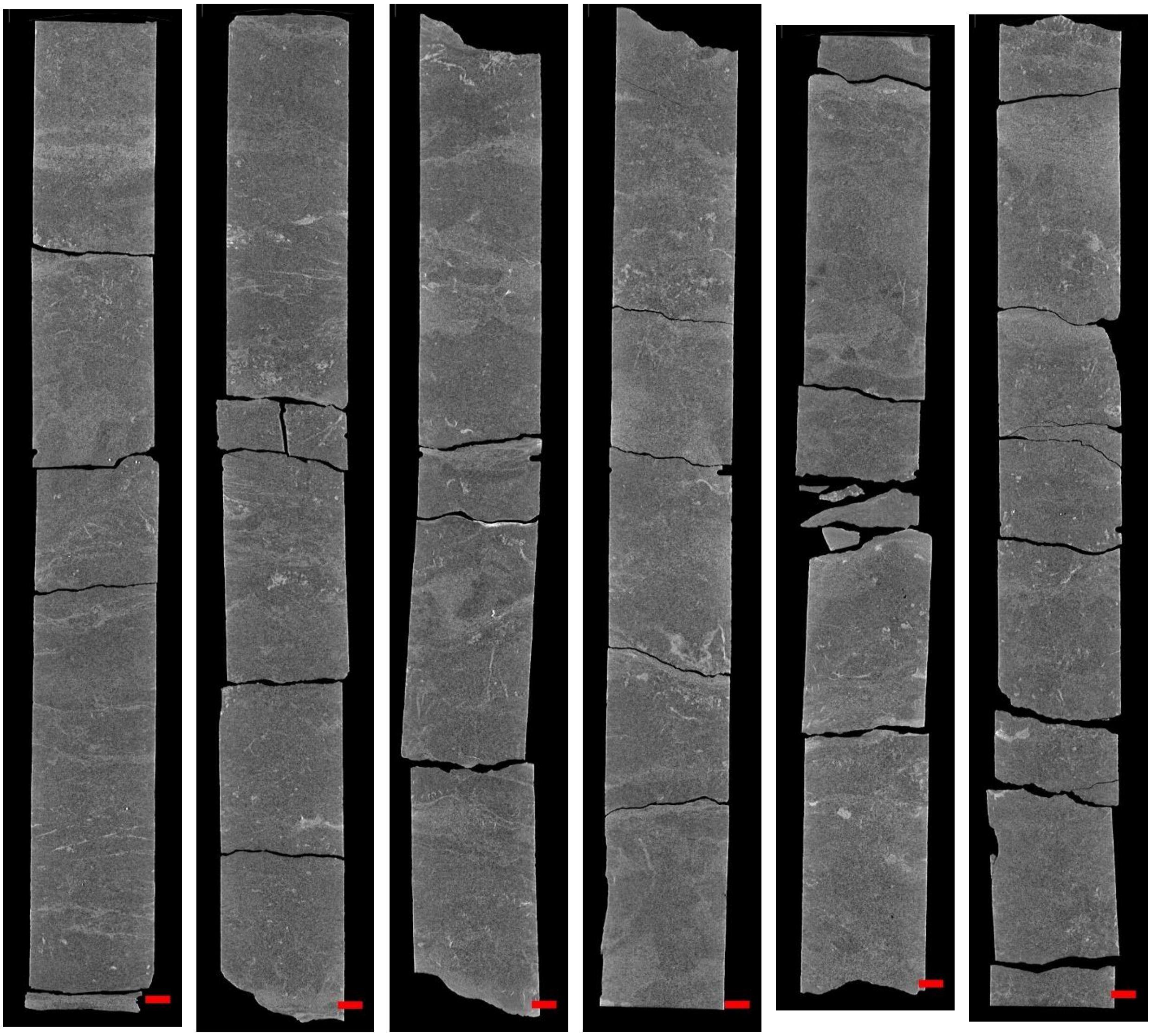

7,999–8,002 ft **8,002–8,005 ft** **8,005–8,008 ft** **8,008–8,011 ft** **8,011–8,014 ft** **8,014–8,017 ft**

Figure 23: 2D isolated planes through the vertical center of the medical CT scans of the Boggess 17H core from 7,999 to 8,017 ft.

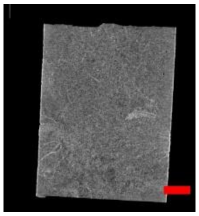

8,017 - 8,017.5 ft

Figure 24: 2D isolated planes through the vertical center of the medical CT scans of the Boggess 17H core from 8,017 to 8,017.5 ft.

4.3 ADDITIONAL CT DATA

Additional CT data can be accessed from NETL's EDX online system using the following link: https://edx.netl.doe.gov/dataset/boggess-17h-well. The original CT data is available as 16-bit tif stacks suitable for reading with ImageJ (Schneider et al., 2012) or other image analysis software.

4.3.1 Medical CT Image Videos

In addition to the CT data, videos showing the variation along the length of the cross-section images shown in the previous section are available for download and viewing on EDX. A single image from these videos is shown in Figure 25, where the distribution of high-density minerals in a cross section of the core from a depth of 7,876 to 7,879 ft is shown. Here, the red line through the XZ-plane on the image of the core shows the location of the XY-plane displayed above. The videos on EDX show this XY variation along the entire length of the core.

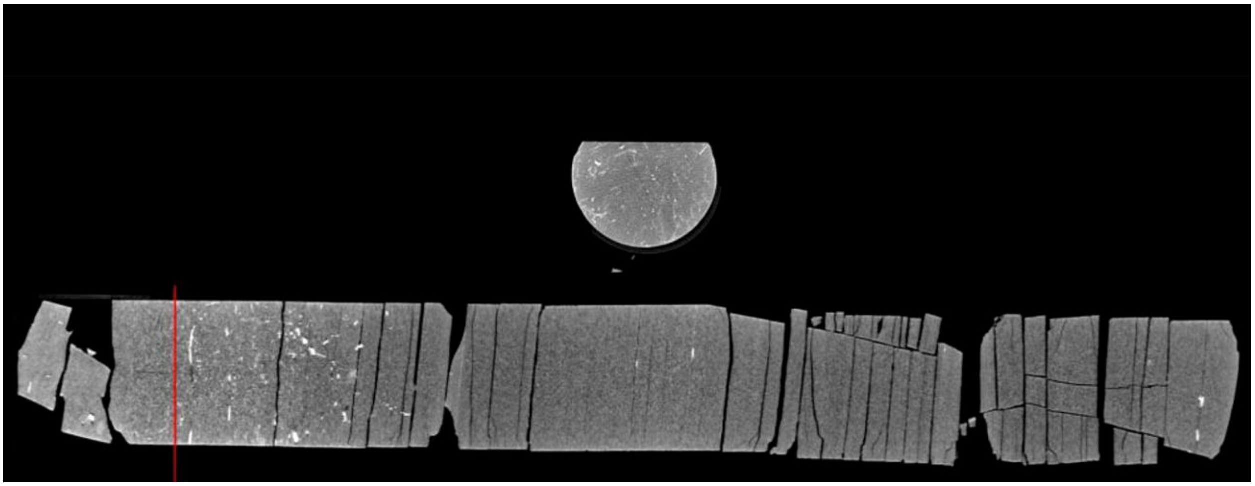

Figure 25: Single image from a video file available on EDX showing variation in the Boggess 17H core from 7,876 to 7,879 ft. This shows the variation in composition within the matrix perpendicular to the core length in this case highlighting burrows in a carbonate interval. Note the bright (high density) concretions in the matrix.

4.3.1 Medical CT Images Sidewall Plugs

Sidewall plugs were scanned in the medical CT scanner at depth intervals listed below (Table 3).

Table 3: List of Sidewall Plug CT Images

Depth	Name
7,488 to 7,920 ft	WC7488_7920.tif
7,924 to 7,995 ft	WC7924_7995.tif
8,000 ft	WC_8000.tif

4.4 DUAL ENERGY CT SCANNING

Dual energy CT scanning uses two sets of images, produced at different X-ray energies, to approximate the density (ρ_B) (Siddiqui and Khamees, 2004; Johnson, 2012). The technique relies on the use of several standards of known ρ_B to be scanned at the same energies as the specimen. These scans are performed at lower energies (<100 KeV) and higher energies (>100 KeV) to induce two types of photon interactions with the object (Figure 26). The lower energy scans induce photoelectric absorption, which occurs when the energy of the photon is completely absorbed by the object mass and causes ejection of an outer orbital electron (Figure 26a). The high energy scans induce Compton scattering, which causes a secondary emission of a lower energy photon due to incomplete absorption of the photon energy in addition to an electron ejection (Figure 26b).

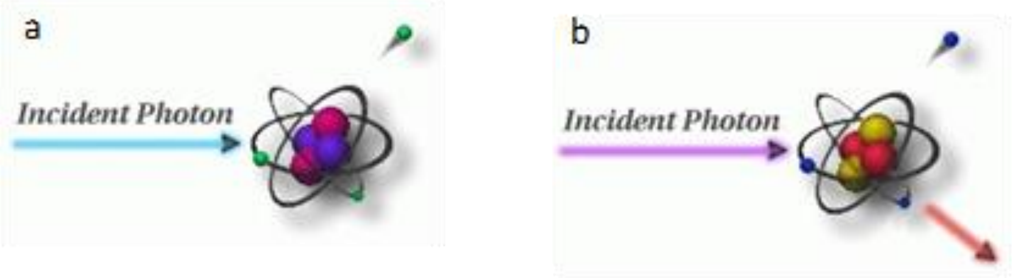

Figure 26: Photon interactions at varying energies: A) Photoelectric absorption, B) Compton scattering. Modified from Iowa State University Center for Nondestructive Evaluation (2021).

Medical grade CT scanners are typically calibrated to known standards, with the output being translated in CT numbers (CTN) or Hounsfield Units (HU). Convention for HU defines air as -1,000 and water as 0. A linear transform of recorded HU values is performed to convert them into CTN. This study used CTN as it is the native export format for the instrument, but it is possible to use HU. Dual energy CT requires at least three calibration points and it is prudent to utilize standards that approximate the object or material of interest. Pure samples of aluminum, graphite, and sodium chloride were used as the calibration standards as they most closely approximate the rocks and minerals of interest (Table 4). Most materials denser than water or with higher atomic masses have a non-linear response to differing CT energies (Table 5).

Table 4: Dual Energy Calibration Standards, Bulk Density (gm/cm^3)

Material	ρ_B (g/cm^3)
Air	-0.001
Water	1
Graphite	2.3
Sodium Chloride	2.16
Aluminum	2.7

Table 5: Dual Energy Calibration Standards, HU, and CTN for "Low" and "High" Energies

Material	HU		CTN	
	80 KeV	135 KeV	80 KeV	135 KeV
Air	-993	-994	31,775	31,774
Water	-3.56	-2.09	32,764	32,766
Graphite	381	437	33,149	33,205
Sodium Chloride	1,846	1,237	34,614	34,005
Aluminum	2,683	2,025	35,451	34,793

Dual energy CT utilizes these differences to calibrate to the X-ray spectra. Two equations with three unknowns each are utilized to find ρ_B (Siddiqui and Khamees, 2004):

$$\rho_B = mCTN_{low} + pCTN_{high} + q$$

Where [m, p, and q] are unknown coefficients that can be solved by setting up a system of equations with four 3 x 3 determinants. The CTN is obtained from the CT scans for each of the homogenous calibration standards.

In this study the high and low energy image stacks were loaded into Python as arrays. A 3D Gaussian blur filter with a sigma of 2 was used to reduce noise in the images. The scipy.solv module of Python was then employed to solve for the coefficients based on the calibration CTN values. The ρ_B was solved for each pixel in the 3D volume and saved as two new separate image stacks.

ImageJ (Rasband, 2019) was used to slice the image stacks to produce 2D representative cross-sections of the entire core-length. A 6-shade look up table was used to apply a gradational color scale to the image with the total range of values limited to densities from 2 to 4.5 g/cm^3; this eliminated much of the noise in the air portion of the scans and at the edges of the sample. The average density along the length of the cores was calculated by excluding all densities below 2 g/cm^3. This study assumed that the cores were free of water and liquids as they were air dried and that the cores do not contain an appreciable quantity of elements with densities lower than 2.0 g/cm^3.

4.5 COMPILED CORE LOG

The compiled core logs were scaled to fit on single pages for rapid review of the combined data from the medical CT scans and MSCL readings. Two sets of logs are presented for the core; the first set with data from the CT scans and XRF, and the second set with calculated ratios and total organic carbon (TOC) from the XRF scans and notable features. Features that can be derived from these combined analyses include determination of mineral locations, such as pyrite, from magnetic susceptibility and using the XRF to inform geochemical composition and mineral form.

The elemental results from the XRF were limited to light elements, Ca, Si, Al, and the remaining top ten elements (Ti, S, Fe, Mn, V, Zr, Zn, Cu, and Cl). Of the remaining top ten elements, Al was the most abundant with a maximum occurrence of 129,192 ppm at one location in the core, and Zr was the least abundant element with a maximum occurrence of 767 ppm at one location in the core. All other elements were measured, but not listed.

Trends in elemental ratios can provide insight into mineral composition, oxidation state, and depositional setting. Examples include: Mn/Fe, which provides insight into the redox state; Ca/Si, which provides information on relative abundance of calcium carbonates versus silicates; Ti/Al, which gives approximate amounts of calcium carbonate versus clays and feldspars; Si/Al, which provides information on the abundance of illite and micas versus other clays; and S/Fe and Fe/Al, which provide information on the abundance of pyrite versus Fe oxide minerals. Additionally, magnetic susceptibility can test for iron sulfides (reducing) or oxidized Fe and sulfate. Pyrite (reduced) should have low magnetic susceptibility; Fe oxide or hydroxide should have high magnetic susceptibility. Natural gamma is a proxy for organic carbon as well. These broad trends can quickly give information on large suites of core and direct more focused research. These logs are presented in Figure 27 and Figure 28.

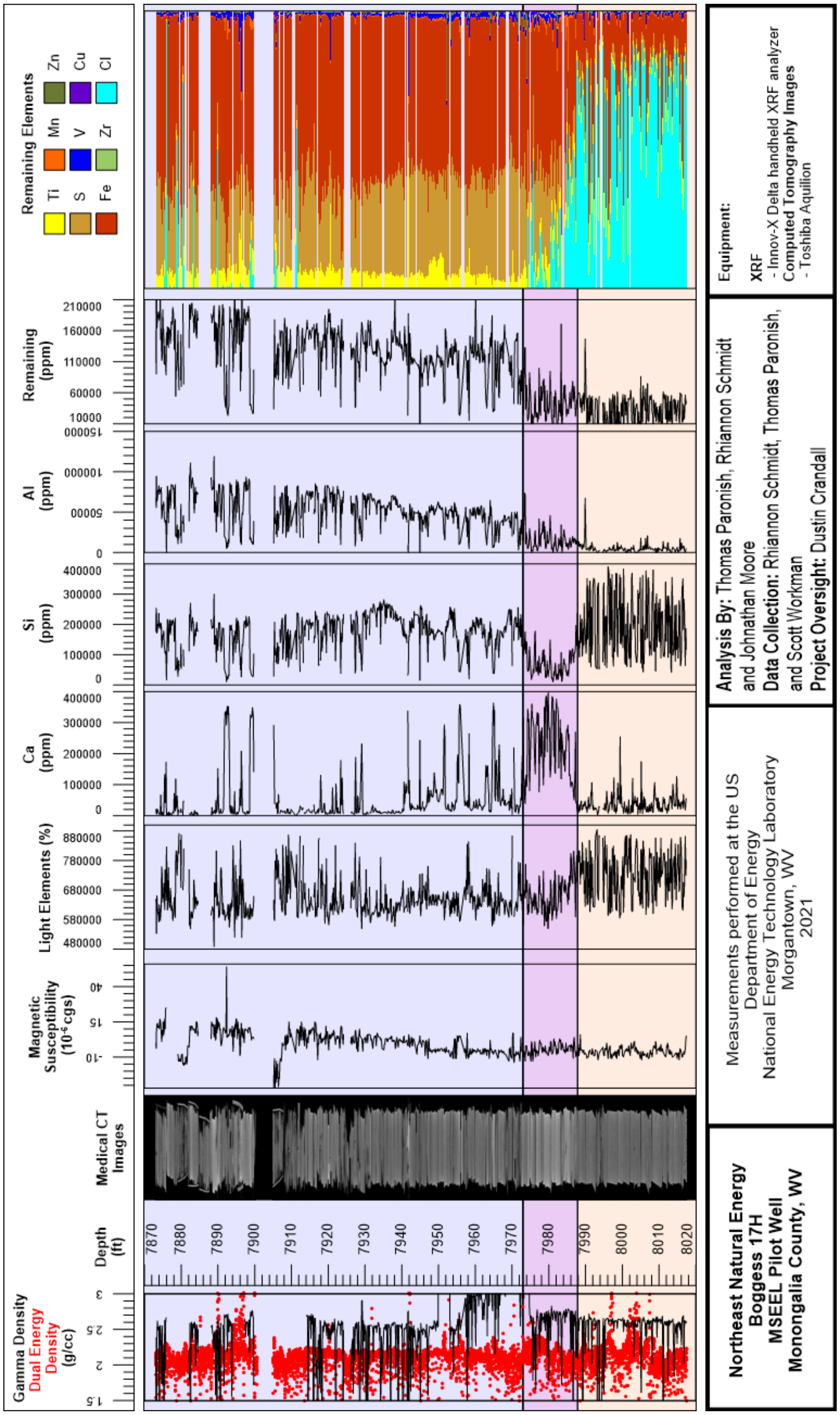

Northeast Natural Energy
Boggess 17H
MSEEL Pilot Well
Monongalia County, WV

Measurements performed at the US Department of Energy National Energy Technology Laboratory Morgantown, WV 2021

Analysis By: Thomas Paronish, Rhiannon Schmidt and Johnathan Moore
Data Collection: Rhiannon Schmidt, Thomas Paronish, and Scott Workman
Project Oversight: Dustin Crandall

Equipment:
XRF
- Innov-X Delta handheld XRF analyzer
Computed Tomography Images
- Toshiba Aquilion

Figure 27: Compiled core log detailing the elemental results; Marcellus Shale (blue), Onondaga Limestone (purple), and Huntersville Chert (orange).

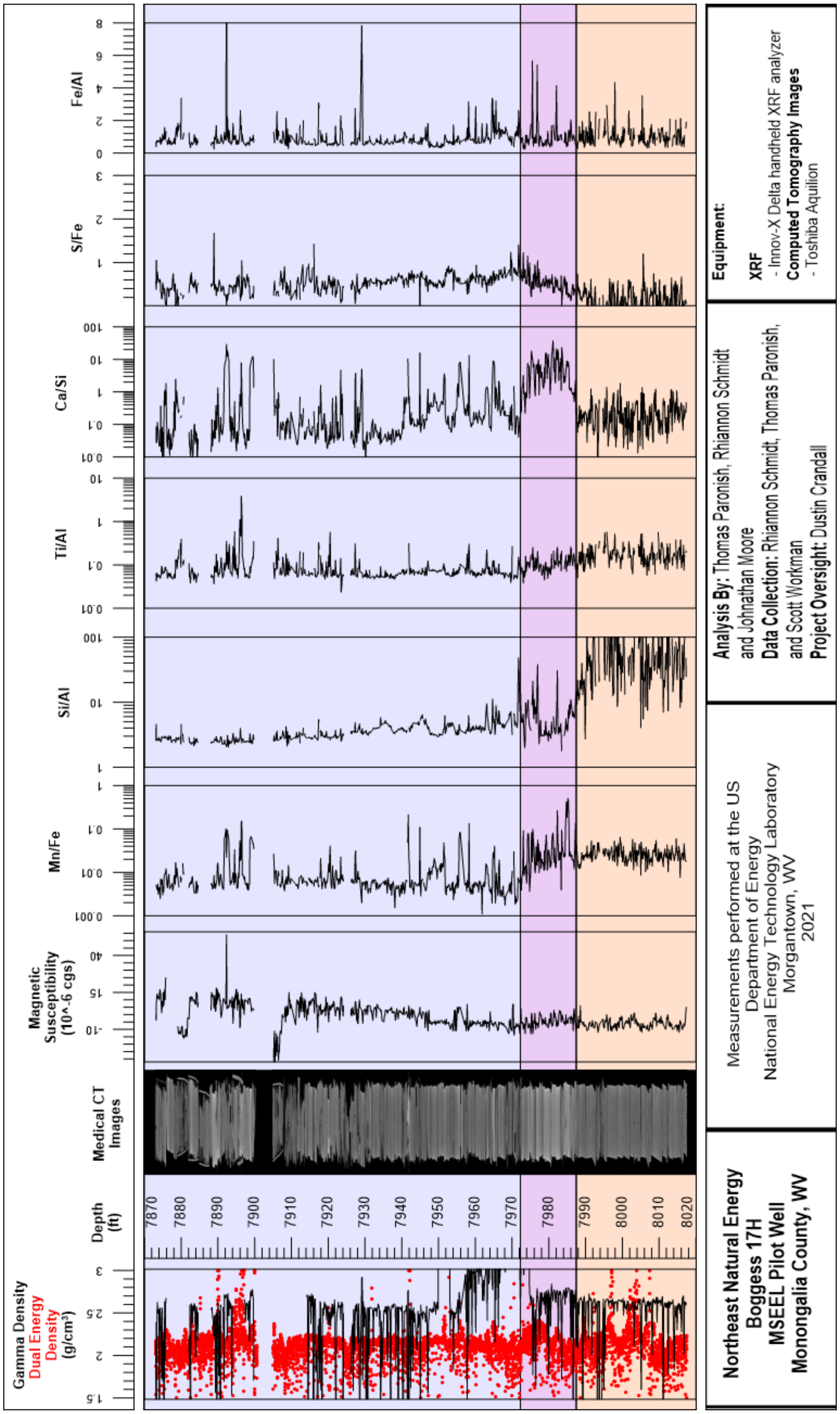

Figure 28: Compiled core log of elemental ratios; Marcellus Shale (blue), Onondaga Limestone (purple), and Huntersville Chert (orange).

5. DISCUSSION

The measurements of the magnetic susceptibility, P-wave velocity, XRF, and CT analysis provide a unique look into of the internal structure of the core and macroscopic changes in lithology. These techniques:

- Are non-destructive.
- When performed in parallel, give insight into the core beyond what one individual technique can provide.
- Can be used to identify zones of interest for detailed analysis, experimentation, and quantification.
- Provide a detailed digital record of the core, before any destructive testing or further degradation, that is accessible and can be referenced for future studies.

This page intentionally left blank.

6. REFERENCES

Cnudde, V.; Boone, M.N. High-resolution X-ray computed tomography in geosciences: A review of the current technology and applications. *Earth-Science Reviews* **2013,** *123*, 1–17.

Crandall, D. MIP3H_Scans, 2018-11-29; 2018. https://edx.netl.doe.gov/dataset/mip3h-scans

EIA. Energy Information Administration (EIA). EIA. Oil and Gas Supply Module. *Assumptions to Annual Energy Outlook 2018*; 2018; pp 1–19.

Geotek Ltd. Multi-Sensor Core Logger Manual; Version 05-10; Published by Geotek, 3 Faraday Close, Daventry, Northamptonshire NN11 8RD, 2010. info@geotek.co.uk, www.geotek.co.uk

Hunts, C.; Moskowitz, B.; Banerjee, S. *Magnetic Properties of Rocks and Minerals;* Rock Physics and Phase Relations: A Handbook of Physical Constants; 1995; p 189–204.

IEDA (Interdisciplinary Earth Data Alliance). SESAR, the System for Earth Sample Registration. Web Page, 2018. http://www.geosamples.org/about (accessed Feb 8, 2018)

Iowa State University Center for Nondestructive Evaluation, Ames, IA, 2021. https://www.nde-ed.org/Physics/X-Ray/attenuation.xhtml (accessed July 2021).

Johnson, T. R. C. Dual-Energy CT: General Principles. *American Journal of Roentgenology* **2012,** *199*(5_supplement), S3–S8. DOI: 10.2214/AJR.12.9116.

Lazar, O. R.; Bohacs, K. M.; Macquaker, J. H.; Schieber, J.; Demko, T. M. Capturing Key Attributes of Fine-Grained Sedimentary Rocks in Outcrops, Cores, and Thin Sections: Nomenclature and Description Guidelines. *Journal of Sedimentary Research* **2015,** *85*, 230–246.

Paronish, T.; Mackey, P.; Crandall, D.; Moore, J.; Brown, S.; Carr, T.; Martin, K. *Computed Tomography Scanning and Geophysical Measurements of Core from the Marcellus Shale Energy and Environment Laboratory*; NETL-TRS-22-2018; NETL Technical Report Series; U.S. Department of Energy, National Energy Technology Laboratory: Morgantown, WV, 2018; p 56. DOI: 10.18141/1488537.

Rasband, W. S. *ImageJ*. U.S. National Institutes of Health: Bethesda, MD, 1997–2019, http://imagej.nih.gov/ij/ (accessed 2019).

Schneider, C. A.; Rasband, W. S.; Eliceiri, K. W. NIH Image to ImageJ: 25 years of image analysis. *Nature Methods* **2012,** *9*, 671–675.

Siddiqui, S.; Khamees, A. A. Dual-Energy CT-Scanning Applications in Rock Characterization. *Society of Petroleum Engineers* **2004**. DOI:10.2118/90520-MS.

This page intentionally left blank.

Brian Anderson
Director
National Energy Technology Laboratory
U.S. Department of Energy

Jared Ciferno
Associate Director
Oil and Gas
Technology Development & Integration Center
National Energy Technology Laboratory
U.S. Department of Energy

David Alman
Acting Director
Division of Upstream Oil and Gas Research
U.S. Department of Energy

Bryan Morreale
Executive Director
Research and Innovation Center
National Energy Technology Laboratory
U.S. Department of Energy

NETL Technical Report Series